



Factors influencing the precision and accuracy of Nd isotope measurements by thermal ionization mass spectrometry

Marion Garçon, Maud Boyet, Richard Carlson, Mary Horan, Delphine Auclair, Timothy Mock

► To cite this version:

Marion Garçon, Maud Boyet, Richard Carlson, Mary Horan, Delphine Auclair, et al.. Factors influencing the precision and accuracy of Nd isotope measurements by thermal ionization mass spectrometry. *Chemical Geology*, 2018, 476, pp.493-514. 10.1016/j.chemgeo.2017.12.003 . hal-01720763

HAL Id: hal-01720763

<https://uca.hal.science/hal-01720763>

Submitted on 5 Mar 2018

HAL is a multi-disciplinary open access archive for the deposit and dissemination of scientific research documents, whether they are published or not. The documents may come from teaching and research institutions in France or abroad, or from public or private research centers.

L'archive ouverte pluridisciplinaire **HAL**, est destinée au dépôt et à la diffusion de documents scientifiques de niveau recherche, publiés ou non, émanant des établissements d'enseignement et de recherche français ou étrangers, des laboratoires publics ou privés.

Factors influencing the precision and accuracy of Nd isotope measurements by thermal ionization mass spectrometry

Marion Garçon^{1,2,3*}, Maud Boyet², Richard W. Carlson³, Mary F. Horan³,
Delphine Auclair², Timothy D. Mock³

Published in Chemical Geology

¹ ETH Zürich, Department of Earth Sciences, Institute of Geochemistry and Petrology, Clausiusstrasse 25, 8092 Zürich, Switzerland

² Université Clermont Auvergne, CNRS, IRD, OPGC, Laboratoire Magmas et Volcans, F-63000 Clermont-Ferrand, France

³ Carnegie Institution for Science, Department of Terrestrial Magnetism, 5241 Broad Branch Road, NW, Washington DC 20015-1305, United States

* Corresponding author

E-mail: marion.garcon@erdw.ethz.ch

Phone: +41 44 632 3745

Present address: ETH Zürich, Department of Earth Sciences, Institute of Geochemistry and Petrology, Clausiusstrasse 25, 8092 Zürich, Switzerland

To cite this paper:

Garçon M., Boyet M., Carlson R.W., Horan M. T., Auclair D., Mock T.D., Factors influencing the precision and accuracy of isotope measurements by thermal ionization mass spectrometry. *Chemical Geology*, 476, 493-514 (2018)

Abstract

Taking the example of Nd, we present a method based on a 4-mass-step acquisition scheme to measure all isotope ratios dynamically by thermal ionization mass spectrometry (TIMS); the aim being to minimize the dependency of all mass fractionation-corrected ratios on collector efficiencies and amplifier gains. The performance of the method was evaluated from unprocessed JNdi-1 Nd standards analyzed in multiple sessions on three different instruments over a period of ~ 1.5 years ($n = 61$), as well as from standards (18 JNdi-1 and 19 BHVO-2) processed through different chemical purification procedures. The Nd isotopic compositions of standards processed through fine-grained (25-50 μm) Ln-spec resin show a subtle but clear fractionation caused by the nuclear field shift effect. This effect contributes to the inaccuracy of Nd isotope measurements at the ppm level of precision.

Following a comprehensive evaluation of the mass spectrometer runs, we suggest several criteria to assess the quality of data acquired by TIMS, in particular to see whether the measurements were affected by domain mixing effects on the filaments. We define maximum tolerable Ce and Sm interference corrections and the minimum number of ratios to acquire to ensure the best possible accuracy and precision for all Nd isotope ratios. Changes in fractionation of Nd isotope ratios in between acquisition steps can result in significant inaccuracy and bias dynamic μ_{142} values by more than 15 ppm. To correct for these effects, we developed a systematic drift-correction based on the monitoring of Nd isotope ratios through time. The residual components of scatter in the JNdi-1 and BHVO-2 datasets were further investigated in binary isotopic plots in which we modeled the theoretical effects of domain mixing on filaments, nuclear field shift and correlated errors from counting statistics using Monte-Carlo simulations. These plots indicate that the 4-step method returns precisions limited by counting errors only for drift-corrected dynamic Nd isotope ratios. Data acquired on three different TIMS instruments suggest the following composition for the JNdi-1 reference standard: $^{142}\text{Nd}/^{144}\text{Nd} = 1.141832 \pm 0.000006$ (2s), $^{143}\text{Nd}/^{144}\text{Nd} = 0.512099 \pm 0.000005$ (2s), $^{145}\text{Nd}/^{144}\text{Nd} = 0.348403 \pm 0.000003$ (2s), $^{148}\text{Nd}/^{144}\text{Nd} = 0.241581 \pm 0.000003$ (2s), and $^{150}\text{Nd}/^{144}\text{Nd} = 0.236452 \pm 0.000006$ (2s) when normalized to $^{146}\text{Nd}/^{144}\text{Nd} = 0.7219$. Measurements performed on different instruments (TritonTM vs. Triton PlusTM) show resolvable differences of about 10 ppm for absolute $^{143}\text{Nd}/^{144}\text{Nd}$, $^{145}\text{Nd}/^{144}\text{Nd}$ and $^{148}\text{Nd}/^{144}\text{Nd}$ ratios. The different criteria and corrections developed in this study could be applied to other isotopic systematics to improve and better evaluate the quality of high-precision data acquired by TIMS.

Keywords: Neodymium, TIMS, dynamic, static, isotopic composition

1. Introduction

Thermal ionization mass spectrometry (TIMS) is the state-of-the-art technique to measure isotope ratios at the ppm precision level provided that the element of interest has the right properties to ionize efficiently (see Carlson, 2014 for a review). The advent of multicollector TIMS allowed isotope ratios to be calculated by simultaneous collection of the ion beams of different masses, reducing the consequences of temporal variations in ion intensity and increasing the amount of signal integration per measurement interval, both of which foster higher precision isotope ratio determinations. The simplest of these methods is so-called static multicollection where all the ion beams are measured simultaneously. To calculate accurate isotope ratios from simultaneously detected ion beams requires knowledge of the amplifier gains and collection efficiencies of each faraday detector used in the measurement. The amplifier gains and faraday efficiencies theoretically can be eliminated through the technique of dynamic multicollection. In this approach, at least two magnet steps are made that move both the target and a standardizing isotope into the same faraday cup. The unknown isotope ratio is then calculated by combining the equations for the unknown ratio and the standardizing ratio in a way where the cup gains and efficiencies divide out. The relative deterioration of faraday collectors and their change of efficiency through time has been pinpointed as an important source of imprecision and inaccuracy for the determination of isotope ratios using static multicollection since the 1990's (Makishima and Nakamura, 1991; Thirlwall, 1991). Similarly, changes in amplifier gain during measurement can affect isotope ratio determinations. The role of amplifier drift has been addressed by electronically rotating amplifiers between faraday cups so that any inaccuracy in the amplifier gains will be averaged over the entire measurement. By minimizing the consequences of relative cup inefficiencies and amplifier gain variability, the dynamic acquisition of isotope ratios avoids the consequences of cup deterioration and amplifier gain changes and yields better long-term precision and accuracy than static multicollection (Carlson, 2014; Fukai et al., 2017; Thirlwall, 1991).

Many studies have used the dynamic technique to investigate the small ^{142}Nd anomalies created by the decay of 103 million year half-life ^{146}Sm in both terrestrial and extra-terrestrial materials. Recent studies typically yield external isotope ratio precisions ranging from 3 to 8 ppm (2s) on the $^{142}\text{Nd}/^{144}\text{Nd}$ ratios of reference standards repeatedly measured through

different analytical sequences (cf. Bouvier and Boyet, 2016; Burkhardt et al., 2016; Carlson et al., 2007; O'Neil et al., 2008; Rizo et al., 2012; Roth et al., 2013). More recently, Burkhardt et al. (2016) and Fukai et al. (2017) used a two mass-step acquisition method to calculate dynamic $^{148}\text{Nd}/^{144}\text{Nd}$ and $^{150}\text{Nd}/^{144}\text{Nd}$ ratios, in addition to $^{142}\text{Nd}/^{144}\text{Nd}$ ratios. Here, we propose a new method based on a 4 mass-step acquisition routine able to return all Nd isotope ratios dynamically, including the radiogenic $^{143}\text{Nd}/^{144}\text{Nd}$ ratio. We investigate the potential sources of imprecision and inaccuracy in the measurement of Nd isotope ratios by TIMS, and additionally suggest corrections to improve the quality of the data as well as criteria to recognize poor-quality runs after acquisition. While the study focuses on Nd, the processes, corrections and recommendations discussed here could potentially be applied to the measurement of other isotopic systems and provide keys to improve both the acquisition and the reduction of high-precision isotopic data in general.

2. The 4 mass-step method: principles and equations

The dynamic measurement of all Nd isotope ratios involves the use of 4 different magnet settings per cycle. Two different mass-step sequences were tested to investigate how the mass fractionation rate affected the measurement of dynamic Nd isotope ratios (cf. Roth et al., 2014). They are shown in Table 1 together with run parameters such as voltages employed in the zoom optics, integration times, and the idle time spent before initiating signal integration after mass steps. The two tested configurations have the same collector positions, with the axial faraday cup successively centered on ^{143}Nd , ^{144}Nd , ^{145}Nd , and ^{146}Nd , and only differ by the order in which the acquisition lines are measured. Each 4-step cycle returns four static ratios for $^{142}\text{Nd}/^{144}\text{Nd}$, $^{143}\text{Nd}/^{144}\text{Nd}$, and $^{145}\text{Nd}/^{144}\text{Nd}$, three static ratios for $^{148}\text{Nd}/^{144}\text{Nd}$, one static ratio for $^{150}\text{Nd}/^{144}\text{Nd}$, two dynamic ratios for $^{142}\text{Nd}/^{144}\text{Nd}$, $^{143}\text{Nd}/^{144}\text{Nd}$, and $^{148}\text{Nd}/^{144}\text{Nd}$, three dynamic ratios for $^{145}\text{Nd}/^{144}\text{Nd}$, and one dynamic $^{150}\text{Nd}/^{144}\text{Nd}$ ratio, all normalized to $^{146}\text{Nd}/^{144}\text{Nd} = 0.7219$.

2.1. Equations for dynamic $^{142}\text{Nd}/^{144}\text{Nd}$ ratios

Dynamic ratios are calculated assuming that Nd mass fractionation follows an exponential law during the run (Andreasen and Sharma, 2009; Upadhyay et al., 2008). The veracity of this assumption for our measurements is re-examined below when evaluating the results in Section 4.1.1.a. The first dynamic $^{142}\text{Nd}/^{144}\text{Nd}$ ratio, $\left(\frac{^{142}\text{Nd}}{^{144}\text{Nd}}\right)_{\text{Dyn 1}}$, is obtained by combining

the $^{142}\text{Nd}/^{144}\text{Nd}$ ratio measured on line 1, $\left(\frac{^{142}\text{Nd}}{^{144}\text{Nd}}\right)_{\text{Meas 1}}$, together with the $^{146}\text{Nd}/^{144}\text{Nd}$ ratio measured on line 3, $\left(\frac{^{146}\text{Nd}}{^{144}\text{Nd}}\right)_{\text{Meas 3}}$, to minimize the difference of efficiencies and amplifier gains between faraday collectors L1 and H1. This gives:

$$\left(\frac{^{142}\text{Nd}}{^{144}\text{Nd}}\right)_{\text{Dyn 1}} = \left(\frac{^{142}\text{Nd}}{^{144}\text{Nd}}\right)_{\text{Meas 1}} \times \left(\frac{m_{142}}{m_{144}}\right)^{F_3} \quad \text{with } F_3 = \frac{\ln\left(\frac{\left(\frac{^{146}\text{Nd}}{^{144}\text{Nd}}\right)_{\text{True}}}{\left(\frac{^{146}\text{Nd}}{^{144}\text{Nd}}\right)_{\text{Meas 3}}}\right)}{\ln\left(\frac{m_{146}}{m_{144}}\right)} \quad (\text{Eq. 1})$$

where m_{142} , m_{144} , and m_{146} are the atomic masses of isotopes ^{142}Nd , ^{144}Nd and ^{146}Nd , respectively; $\left(\frac{^{146}\text{Nd}}{^{144}\text{Nd}}\right)_{\text{True}} = 0.7219$ is the normalizing ratio used for mass fractionation correction. Given that the measured ion-beam intensities depend on the collector efficiencies and amplifier gains, we can write:

$$\left(\frac{^{142}\text{Nd}}{^{144}\text{Nd}}\right)_{\text{Meas 1}} = \frac{I^{142}\text{Nd}_{\text{Meas 1}}}{I^{144}\text{Nd}_{\text{Meas 1}}} = \frac{I^{142}\text{Nd}_1 \times C_{L1} \times G_{L1}}{I^{144}\text{Nd}_1 \times C_{H1} \times G_{H1}}$$

and $\left(\frac{^{146}\text{Nd}}{^{144}\text{Nd}}\right)_{\text{Meas 3}} = \frac{I^{146}\text{Nd}_{\text{Meas 3}}}{I^{144}\text{Nd}_{\text{Meas 3}}} = \frac{I^{146}\text{Nd}_3 \times C_{H1} \times G_{H1}}{I^{144}\text{Nd}_3 \times C_{L1} \times G_{L1}}$

where $I^{142}\text{Nd}_1$, $I^{144}\text{Nd}_1$, $I^{146}\text{Nd}_3$, and $I^{144}\text{Nd}_3$ are the “ true ” intensities of the different Nd isotope beams on acquisition lines 1 and 3; C_{L1} and C_{H1} are the efficiencies of the faraday collectors L1 and H1 that change with time depending on instrument use; G_{L1} and G_{H1} are the gains of the amplifiers to which the faraday collectors L1 and H1 are attached. Using this notation, (Eq.1) can be re-written as follows:

$$\left(\frac{^{142}\text{Nd}}{^{144}\text{Nd}}\right)_{\text{Dyn 1}} = \frac{I^{142}\text{Nd}_1 \times C_{L1} \times G_{L1}}{I^{144}\text{Nd}_1 \times C_{H1} \times G_{H1}} \times \exp\left(\frac{\ln\left(\frac{\left(\frac{^{146}\text{Nd}}{^{144}\text{Nd}}\right)_{\text{True}}}{\frac{I^{146}\text{Nd}_3 \times C_{H1} \times G_{H1}}{I^{144}\text{Nd}_3 \times C_{L1} \times G_{L1}}}\right)}{\ln\left(\frac{m_{146}}{m_{144}}\right)} \times \ln\left(\frac{m_{142}}{m_{144}}\right)\right)$$

$$\Leftrightarrow \left(\frac{^{142}\text{Nd}}{^{144}\text{Nd}}\right)_{\text{Dyn 1}} = \frac{I^{142}\text{Nd}_1 \times C_{L1} \times G_{L1}}{I^{144}\text{Nd}_1 \times C_{H1} \times G_{H1}} \times \left(\frac{\left(\frac{^{146}\text{Nd}}{^{144}\text{Nd}}\right)_{\text{True}}}{\frac{I^{146}\text{Nd}_3 \times C_{H1} \times G_{H1}}{I^{144}\text{Nd}_3 \times C_{L1} \times G_{L1}}}\right)^{\varphi} \quad \text{with } \varphi = \frac{\ln\left(\frac{m_{142}}{m_{144}}\right)}{\ln\left(\frac{m_{146}}{m_{144}}\right)}$$

$$\Leftrightarrow \left(\frac{^{142}\text{Nd}}{^{144}\text{Nd}}\right)_{\text{Dyn 1}} = \frac{I^{142}\text{Nd}_1}{I^{144}\text{Nd}_1} \times \left(\frac{^{146}\text{Nd}}{^{144}\text{Nd}}\right)_{\text{True}}^{\varphi} \times \left(\frac{I^{146}\text{Nd}_3}{I^{144}\text{Nd}_3}\right)^{-\varphi} \times \left(\frac{C_{L1} \times G_{L1}}{C_{H1} \times G_{H1}}\right)^{1+\varphi} \quad (\text{Eq. 2})$$

Using $m_{142} = 141.907729$; $m_{144} = 143.910093$ and $m_{146} = 145.913123$ (AME2012, Wang et al.(2012)), φ is equal to -1.013677, hence the faraday cup efficiencies and amplifier gains (i.e. $\frac{C_{L1} \times G_{L1}}{C_{H1} \times G_{H1}}$) almost divide out completely in (Eq.2). This means that the calculation of dynamic ratios mathematically reduces the non-ideal behavior of both the faraday collectors and the amplifier gains to a negligible contribution compared to the contribution they have on a static ratio. Indeed, following the same notation, the static $\left(\frac{^{142}\text{Nd}}{^{144}\text{Nd}}\right)$ ratio from acquisition line 1 corresponds to:

$$\left(\frac{^{142}\text{Nd}}{^{144}\text{Nd}}\right)_{\text{Static 1}} = \frac{I^{142}\text{Nd}_1}{I^{144}\text{Nd}_1} \times \left(\frac{^{146}\text{Nd}}{^{144}\text{Nd}}\right)_{\text{True}}^{\varphi} \times \left(\frac{I^{146}\text{Nd}_1}{I^{144}\text{Nd}_1}\right)^{-\varphi} \times \frac{C_{L1} \times G_{L1}}{C_{H1} \times G_{H1}} \times \left(\frac{C_{H3} \times G_{H3}}{C_{H1} \times G_{H1}}\right)^{-\varphi}$$

The relative difference between the static ratio from acquisition line 1 and the true value $\left(\frac{^{142}\text{Nd}}{^{144}\text{Nd}}\right)_{\text{True}}$, that is the ideal case for which the faraday collector efficiencies C and the amplifier gains G are all equal to 1, can be expressed in ppm as follows:

$$\mu_{\text{Stat 1}} = \left(\frac{\left(\frac{^{142}\text{Nd}}{^{144}\text{Nd}}\right)_{\text{Static 1}}}{\left(\frac{^{142}\text{Nd}}{^{144}\text{Nd}}\right)_{\text{True}}} - 1 \right) \times 10^6 = \left(\frac{C_{L1}}{C_{H1}} \times \left(\frac{C_{H3}}{C_{H1}}\right)^{-\varphi} \times \frac{G_{L1}}{G_{H1}} \times \left(\frac{G_{H3}}{G_{H1}}\right)^{-\varphi} - 1 \right) \times 10^6$$

Similarly, the relative difference between the first dynamic ratio and the true value is:

$$\mu_{\text{Dyn 1}} = \left(\frac{\left(\frac{^{142}\text{Nd}}{^{144}\text{Nd}}\right)_{\text{Dyn 1}}}{\left(\frac{^{142}\text{Nd}}{^{144}\text{Nd}}\right)_{\text{True}}} - 1 \right) \times 10^6 = \left(\left(\frac{C_{L1}}{C_{H1}}\right)^{1+\varphi} \times \left(\frac{G_{L1}}{G_{H1}}\right)^{1+\varphi} - 1 \right) \times 10^6$$

Because $\varphi \sim -1$, one can see that $\mu_{\text{Dyn 1}}$ will always be close to zero while $\mu_{\text{Stat 1}}$ will scale to $\sim \frac{C_{L1}}{C_{H3} \times C_{H1}^2} \times \frac{G_{L1}}{G_{H3} \times G_{H1}^2}$. One consequence of this result is that the precise calibration of the amplifier gains is less critical when measuring dynamic ratios than it is for static ratios; nevertheless, we calibrate the gains every 24h to ensure the best possible accuracy and precision for our dynamic isotope measurements (see section 3.2.). Note also that the electronic rotation of the amplifiers at the end of a block that is available in the Triton software can help to decrease the contribution of $\frac{G_{L1}}{G_{H3} \times G_{H1}^2}$ for the static ratio under the conditions that each isotope is measured with every amplifier through the course of the run. Since the faraday collectors cannot be physically rotated, their efficiencies C , however, will always be an additional source of inaccuracy and imprecision in the acquisition of static and multistatic ratios compared to dynamic ratios.

As previously discussed by Roth et al. (2014), the fact that φ is not strictly equal to -1 implies that dynamic ratios also are not totally immune from collector inefficiencies and amplifier gains. The long-term accuracy of dynamic ratios should thus degrade slowly through time as collector performance deteriorates. Assuming that the amplifier gains are properly calibrated and do not vary during a run (i.e. $G_{H1} = G_{L1} = G_{H3} = 1$), a simple sensitivity test shows that if faraday collector L1 deteriorates faster than faraday collectors H1 and H3 so that $\frac{C_{L1}}{C_{H1}} = 0.999900$ and $\frac{C_{H3}}{C_{H1}} = 1$, then the static $\left(\frac{^{142}\text{Nd}}{^{144}\text{Nd}}\right)$ ratio will be shifted by $\mu_{Stat\ 1} = -100$ ppm while the dynamic $\left(\frac{^{142}\text{Nd}}{^{144}\text{Nd}}\right)$ ratio will only be biased by $\mu_{Dyn\ 1} = +1.4$ ppm relative to the true value. In percentage, this means that $\sim 98.6\%$ of the faraday collector effects are removed by the dynamic acquisition scheme.

Given the 4-line acquisition scheme, combining steps 2 and 4 provides another dynamic $^{142}\text{Nd}/^{144}\text{Nd}$ ratio that removes $\sim 98.6\%$ of the relative cup efficiencies and amplifier gains of collectors L2 and Ax. This second dynamic ratio can be expressed as :

$$\left(\frac{^{142}\text{Nd}}{^{144}\text{Nd}}\right)_{\text{Dyn 2}} = \left(\frac{^{142}\text{Nd}}{^{144}\text{Nd}}\right)_{\text{Meas 2}} \times \left(\frac{^{146}\text{Nd}}{^{144}\text{Nd}}\right)_{\text{True}}^{\varphi} \times \left(\frac{^{146}\text{Nd}}{^{144}\text{Nd}}\right)_{\text{Meas 4}}^{-\varphi} \quad (\text{Eq. 3})$$

Or, in more detail:

$$\left(\frac{^{142}\text{Nd}}{^{144}\text{Nd}}\right)_{\text{Dyn 2}} = \left(\frac{I^{142}\text{Nd}_2}{I^{144}\text{Nd}_2}\right) \times \left(\frac{^{146}\text{Nd}}{^{144}\text{Nd}}\right)_{\text{True}}^{\varphi} \times \left(\frac{I^{146}\text{Nd}_4}{I^{144}\text{Nd}_4}\right)^{-\varphi} \times \left(\frac{C_{L2} \times G_{L2}}{C_{Ax} \times G_{Ax}}\right)^{1+\varphi}$$

The 4-line configuration thus allows the determination of two independent dynamic $^{142}\text{Nd}/^{144}\text{Nd}$ ratios per cycle. Therefore, even if a 4-line cycle lasts twice as long as a 2-line cycle, the total signal acquisition time of a run is nearly the same as for the common 2-line method line to get a given number of dynamic ratios. For example, aiming to get 1000 $^{142}\text{Nd}/^{144}\text{Nd}$ dynamic ratios per run would require the acquisition of 1000 cycles with the common 2-line method and only 500 cycles with the 4-line method because each cycle produces two independent $^{142}\text{Nd}/^{144}\text{Nd}$ dynamic ratios.

2.2. Equations for dynamic $^{143}\text{Nd}/^{144}\text{Nd}$ ratios

Using the same principles as above, we combine ratios measured on steps 1-2-3 and 2-3-4 to calculate the two dynamic $^{143}\text{Nd}/^{144}\text{Nd}$ ratios. The first dynamic $^{143}\text{Nd}/^{144}\text{Nd}$ ratio, $\left(\frac{^{143}\text{Nd}}{^{144}\text{Nd}}\right)_{\text{Dyn 1}}$, is obtained by multiplying the $^{143}\text{Nd}/^{144}\text{Nd}$ ratio measured on line 1,

$\left(\frac{^{143}\text{Nd}}{^{144}\text{Nd}}\right)_{\text{Meas 1}}$, by the one measured on line 2, $\left(\frac{^{143}\text{Nd}}{^{144}\text{Nd}}\right)_{\text{Meas 2}}$, to cancel out the efficiency and gain of the axial collector, and then by using the $^{146}\text{Nd}/^{144}\text{Nd}$ ratio measured on line 3, $\left(\frac{^{146}\text{Nd}}{^{144}\text{Nd}}\right)_{\text{Meas 3}}$, to correct for mass fractionation. This gives:

$$\left(\frac{^{143}\text{Nd}}{^{144}\text{Nd}}\right)_{\text{Dyn 1}} = \sqrt{\left(\frac{^{143}\text{Nd}}{^{144}\text{Nd}}\right)_{\text{Meas 1}} \times \left(\frac{^{143}\text{Nd}}{^{144}\text{Nd}}\right)_{\text{Meas 2}} \times \left(\frac{m_{143}}{m_{144}}\right)^{2F_3}}$$

$$\text{with } F_3 = \frac{\ln\left(\frac{\left(\frac{^{146}\text{Nd}}{^{144}\text{Nd}}\right)_{\text{True}}}{\left(\frac{^{146}\text{Nd}}{^{144}\text{Nd}}\right)_{\text{Meas 3}}}\right)}{\ln\left(\frac{m_{146}}{m_{144}}\right)}$$

that can be re-written as:

$$\left(\frac{^{143}\text{Nd}}{^{144}\text{Nd}}\right)_{\text{Dyn 1}} = \left(\frac{^{143}\text{Nd}}{^{144}\text{Nd}}\right)_{\text{Meas 1}}^{\frac{1}{2}} \times \left(\frac{^{143}\text{Nd}}{^{144}\text{Nd}}\right)_{\text{Meas 2}}^{\frac{1}{2}} \times \left(\frac{^{146}\text{Nd}}{^{144}\text{Nd}}\right)_{\text{True}}^{\gamma} \times \left(\frac{^{146}\text{Nd}}{^{144}\text{Nd}}\right)_{\text{Meas 3}}^{-\gamma} \quad (\text{Eq. 4})$$

$$= \left(\frac{I^{143}\text{Nd}_1}{I^{144}\text{Nd}_1}\right)^{\frac{1}{2}} \times \left(\frac{I^{143}\text{Nd}_2}{I^{144}\text{Nd}_2}\right)^{\frac{1}{2}} \times \left(\frac{^{146}\text{Nd}}{^{144}\text{Nd}}\right)_{\text{True}}^{\gamma} \times \left(\frac{I^{146}\text{Nd}_3}{I^{144}\text{Nd}_3}\right)^{-\gamma} \times \left(\frac{C_{L1} \times G_{L1}}{C_{H1} \times G_{H1}}\right)^{\frac{1}{2}+\gamma}$$

$$\text{with } \gamma = \frac{\ln\left(\frac{m_{143}}{m_{144}}\right)}{\ln\left(\frac{m_{146}}{m_{144}}\right)}$$

Using $m_{143} = 142.909820$; $m_{144} = 143.910093$ and $m_{146} = 145.913123$ (AME2012, Wang et al.(2012)), $\gamma = -0.504603$. A variation of +100 ppm of the $\frac{C_{L1} \times G_{L1}}{C_{H1} \times G_{H1}}$ ratio produces an increase of $\sim +0.5$ ppm of the dynamic $^{143}\text{Nd}/^{144}\text{Nd}$ ratio, cancelling out $\sim 99.5\%$ of the relative cup efficiencies and gains between H1 and L1. The dynamic measurement of $^{143}\text{Nd}/^{144}\text{Nd}$ ratios is thus slightly more efficient in removing the relative cup gains and efficiencies than the dynamic $^{142}\text{Nd}/^{144}\text{Nd}$ ratios.

We derive a second dynamic $^{143}\text{Nd}/^{144}\text{Nd}$ ratio combining steps 2-3-4 to reduce relative efficiencies and gains between faraday cups L2 and Ax by $\sim 99.5\%$:

$$\left(\frac{^{143}\text{Nd}}{^{144}\text{Nd}}\right)_{\text{Dyn 2}} = \left(\frac{^{143}\text{Nd}}{^{144}\text{Nd}}\right)_{\text{Meas 2}}^{\frac{1}{2}} \times \left(\frac{^{143}\text{Nd}}{^{144}\text{Nd}}\right)_{\text{Meas 3}}^{\frac{1}{2}} \times \left(\frac{^{146}\text{Nd}}{^{144}\text{Nd}}\right)_{\text{True}}^{\gamma} \times \left(\frac{^{146}\text{Nd}}{^{144}\text{Nd}}\right)_{\text{Meas 4}}^{-\gamma} \quad (\text{Eq. 5})$$

$$= \left(\frac{I^{143}\text{Nd}_2}{I^{144}\text{Nd}_2}\right)^{\frac{1}{2}} \times \left(\frac{I^{143}\text{Nd}_3}{I^{144}\text{Nd}_3}\right)^{\frac{1}{2}} \times \left(\frac{^{146}\text{Nd}}{^{144}\text{Nd}}\right)_{\text{True}}^{\gamma} \times \left(\frac{I^{146}\text{Nd}_4}{I^{144}\text{Nd}_4}\right)^{-\gamma} \times \left(\frac{C_{L2} \times G_{L2}}{C_{Ax} \times G_{Ax}}\right)^{\frac{1}{2}+\gamma}$$

2.3. Equations for dynamic $^{145}\text{Nd}/^{144}\text{Nd}$ ratios

The calculation of the three dynamic $^{145}\text{Nd}/^{144}\text{Nd}$ ratios is very similar to that of the dynamic $^{143}\text{Nd}/^{144}\text{Nd}$ ratios. They result from the combination of ratios measured on lines 1-2, 2-3 and 3-4 as shown below:

$$\begin{aligned} \left(\frac{^{145}\text{Nd}}{^{144}\text{Nd}}\right)_{\text{Dyn 1}} &= \left(\frac{^{145}\text{Nd}}{^{144}\text{Nd}}\right)_{\text{Meas 1}}^{\frac{1}{2}} \times \left(\frac{^{145}\text{Nd}}{^{144}\text{Nd}}\right)_{\text{Meas 2}}^{\frac{1}{2}} \times \left(\frac{^{146}\text{Nd}}{^{144}\text{Nd}}\right)_{\text{True}}^{\varpi} \times \left(\frac{^{146}\text{Nd}}{^{144}\text{Nd}}\right)_{\text{Meas 2}}^{-\varpi} \quad (\text{Eq. 6}) \\ &= \left(\frac{I^{145}\text{Nd}_1}{I^{144}\text{Nd}_1}\right)^{\frac{1}{2}} \times \left(\frac{I^{145}\text{Nd}_2}{I^{144}\text{Nd}_2}\right)^{\frac{1}{2}} \times \left(\frac{^{146}\text{Nd}}{^{144}\text{Nd}}\right)_{\text{True}}^{\varpi} \times \left(\frac{I^{146}\text{Nd}_2}{I^{144}\text{Nd}_2}\right)^{-\varpi} \times \left(\frac{C_{\text{H2}} \times G_{\text{H2}}}{C_{\text{Ax}} \times G_{\text{Ax}}}\right)^{\frac{1}{2}-\varpi} \end{aligned}$$

$$\begin{aligned} \left(\frac{^{145}\text{Nd}}{^{144}\text{Nd}}\right)_{\text{Dyn 2}} &= \left(\frac{^{145}\text{Nd}}{^{144}\text{Nd}}\right)_{\text{Meas 2}}^{\frac{1}{2}} \times \left(\frac{^{145}\text{Nd}}{^{144}\text{Nd}}\right)_{\text{Meas 3}}^{\frac{1}{2}} \times \left(\frac{^{146}\text{Nd}}{^{144}\text{Nd}}\right)_{\text{True}}^{\varpi} \times \left(\frac{^{146}\text{Nd}}{^{144}\text{Nd}}\right)_{\text{Meas 3}}^{-\varpi} \quad (\text{Eq. 7}) \\ &= \left(\frac{I^{145}\text{Nd}_2}{I^{144}\text{Nd}_2}\right)^{\frac{1}{2}} \times \left(\frac{I^{145}\text{Nd}_3}{I^{144}\text{Nd}_3}\right)^{\frac{1}{2}} \times \left(\frac{^{146}\text{Nd}}{^{144}\text{Nd}}\right)_{\text{True}}^{\varpi} \times \left(\frac{I^{146}\text{Nd}_3}{I^{144}\text{Nd}_3}\right)^{-\varpi} \times \left(\frac{C_{\text{H1}} \times G_{\text{H1}}}{C_{\text{L1}} \times G_{\text{L1}}}\right)^{\frac{1}{2}-\varpi} \end{aligned}$$

$$\begin{aligned} \left(\frac{^{145}\text{Nd}}{^{144}\text{Nd}}\right)_{\text{Dyn 3}} &= \left(\frac{^{145}\text{Nd}}{^{144}\text{Nd}}\right)_{\text{Meas 3}}^{\frac{1}{2}} \times \left(\frac{^{145}\text{Nd}}{^{144}\text{Nd}}\right)_{\text{Meas 4}}^{\frac{1}{2}} \times \left(\frac{^{146}\text{Nd}}{^{144}\text{Nd}}\right)_{\text{True}}^{\varpi} \times \left(\frac{^{146}\text{Nd}}{^{144}\text{Nd}}\right)_{\text{Meas 4}}^{-\varpi} \quad (\text{Eq. 8}) \\ &= \left(\frac{I^{145}\text{Nd}_3}{I^{144}\text{Nd}_3}\right)^{\frac{1}{2}} \times \left(\frac{I^{145}\text{Nd}_4}{I^{144}\text{Nd}_4}\right)^{\frac{1}{2}} \times \left(\frac{^{146}\text{Nd}}{^{144}\text{Nd}}\right)_{\text{True}}^{\varpi} \times \left(\frac{I^{146}\text{Nd}_4}{I^{144}\text{Nd}_4}\right)^{-\varpi} \times \left(\frac{C_{\text{Ax}} \times G_{\text{Ax}}}{C_{\text{L2}} \times G_{\text{L2}}}\right)^{\frac{1}{2}-\varpi} \end{aligned}$$

$$\text{with } \varpi = \frac{\ln\left(\frac{m_{145}}{m_{144}}\right)}{\ln\left(\frac{m_{146}}{m_{144}}\right)}$$

Using $m_{145} = 142.912579$; $m_{144} = 143.910093$ and $m_{146} = 145.913123$ (AME2012, Wang et al.(2012)), $\varpi = 0.502213$. Dynamic $^{145}\text{Nd}/^{144}\text{Nd}$ ratios are the most efficient in cancelling out the relative difference in cup efficiencies and gains, reducing it by $\sim 99.8\%$. Therefore a variation of +100 ppm of the $\frac{C_{\text{H1}}}{C_{\text{L1}}}$ ratio generates a decrease of ~ 0.2 ppm of the second dynamic $^{145}\text{Nd}/^{144}\text{Nd}$ ratio.

2.4. Equations for dynamic $^{148}\text{Nd}/^{144}\text{Nd}$ ratios

The two dynamic $^{148}\text{Nd}/^{144}\text{Nd}$ ratios are calculated in a slightly different way, using measured $^{148}\text{Nd}/^{146}\text{Nd}$ ratios as in Fukai et al.(2017). Combining ratios measured on lines 1 and 3 gives:

$$\left(\frac{^{148}\text{Nd}}{^{144}\text{Nd}}\right)_{\text{Dyn 1}} = \left(\frac{^{148}\text{Nd}}{^{146}\text{Nd}}\right)_{\text{Meas 3}} \times \left(\frac{^{146}\text{Nd}}{^{144}\text{Nd}}\right)_{\text{True}} \times \left(\frac{m_{148}}{m_{146}}\right)^{F_1}$$

$$\text{with } F_1 = \frac{\ln \left(\frac{\left(\frac{^{146}\text{Nd}}{^{144}\text{Nd}} \right)_{\text{True}}}{\left(\frac{^{146}\text{Nd}}{^{144}\text{Nd}} \right)_{\text{Meas 1}}} \right)}{\ln \left(\frac{m_{146}}{m_{144}} \right)}$$

Hence,

$$\begin{aligned} \left(\frac{^{148}\text{Nd}}{^{144}\text{Nd}} \right)_{\text{Dyn 1}} &= \left(\frac{^{148}\text{Nd}}{^{146}\text{Nd}} \right)_{\text{Meas 3}} \times \left(\frac{^{146}\text{Nd}}{^{144}\text{Nd}} \right)_{\text{True}}^{1+\theta} \times \left(\frac{^{146}\text{Nd}}{^{144}\text{Nd}} \right)_{\text{Meas 1}}^{-\theta} \quad (\text{Eq. 9}) \\ &= \left(\frac{I^{148}\text{Nd}_3}{I^{146}\text{Nd}_3} \right) \times \left(\frac{^{146}\text{Nd}}{^{144}\text{Nd}} \right)_{\text{True}}^{1+\theta} \times \left(\frac{I^{146}\text{Nd}_1}{I^{144}\text{Nd}_1} \right)^{-\theta} \times \left(\frac{C_{\text{H3}} \times G_{\text{H3}}}{C_{\text{H1}} \times G_{\text{H1}}} \right)^{1-\theta} \\ \text{with } \theta &= \frac{\ln \left(\frac{m_{148}}{m_{146}} \right)}{\ln \left(\frac{m_{146}}{m_{144}} \right)} \end{aligned}$$

Similarly, we can combine lines 2 and 4 to obtain a second dynamic ratio:

$$\begin{aligned} \left(\frac{^{148}\text{Nd}}{^{144}\text{Nd}} \right)_{\text{Dyn 2}} &= \left(\frac{^{148}\text{Nd}}{^{146}\text{Nd}} \right)_{\text{Meas 4}} \times \left(\frac{^{146}\text{Nd}}{^{144}\text{Nd}} \right)_{\text{True}}^{1+\theta} \times \left(\frac{^{146}\text{Nd}}{^{144}\text{Nd}} \right)_{\text{Meas 2}}^{-\theta} \quad (\text{Eq. 10}) \\ &= \left(\frac{I^{148}\text{Nd}_4}{I^{146}\text{Nd}_4} \right) \times \left(\frac{^{146}\text{Nd}}{^{144}\text{Nd}} \right)_{\text{True}}^{1+\theta} \times \left(\frac{I^{146}\text{Nd}_2}{I^{144}\text{Nd}_2} \right)^{-\theta} \times \left(\frac{C_{\text{H2}} \times G_{\text{H2}}}{C_{\text{Ax}} \times G_{\text{Ax}}} \right)^{1-\theta} \end{aligned}$$

$\theta = 0.986731$ using $m_{148} = 147.916899$; $m_{144} = 143.910093$ and $m_{146} = 145.913123$ (AME2012, Wang et al.(2012)). This means that dynamic $^{148}\text{Nd}/^{144}\text{Nd}$ ratios reduce the relative difference in cup efficiencies and gains by $\sim 98.7\%$.

2.5. Equations for dynamic $^{150}\text{Nd}/^{144}\text{Nd}$ ratios

The calculation of the dynamic $^{150}\text{Nd}/^{144}\text{Nd}$ ratio is less straightforward than other dynamic ratios as it involves the efficiencies and gains of three cups while the other dynamic ratios involved only two cups. This also means that the dynamic $^{150}\text{Nd}/^{144}\text{Nd}$ ratio will be more affected by cup aging and deterioration. Note that the way we calculate dynamic $^{150}\text{Nd}/^{144}\text{Nd}$ ratios is different from Fukai et al.(2017). The latter used ratios measured in four different cups and involved the measured $^{142}\text{Nd}/^{144}\text{Nd}$ ratio while our calculations rely on three cups only and do not use ^{142}Nd . Only one dynamic $^{150}\text{Nd}/^{144}\text{Nd}$ ratio can be calculated with our cup configuration. Combining ratios from steps 1 and 3 gives:

$$\left(\frac{^{150}\text{Nd}}{^{144}\text{Nd}} \right)_{\text{Dyn 1}} = \left(\frac{^{150}\text{Nd}}{^{146}\text{Nd}} \right)_{\text{Meas 3}} \times \left(\frac{^{146}\text{Nd}}{^{144}\text{Nd}} \right)_{\text{True}} \times \left(\frac{m_{150}}{m_{146}} \right)^{F_1'}$$

$$\text{with } F_1' = \frac{\ln \left(\frac{\left(\frac{^{148}\text{Nd}}{^{144}\text{Nd}} \right)_{\text{Dyn 1}}}{\left(\frac{^{148}\text{Nd}}{^{144}\text{Nd}} \right)_{\text{Meas 1}}} \right)}{\ln \left(\frac{m_{148}}{m_{144}} \right)}$$

Hence,

$$\left(\frac{^{150}\text{Nd}}{^{144}\text{Nd}} \right)_{\text{Dyn 1}} = \left(\frac{^{150}\text{Nd}}{^{146}\text{Nd}} \right)_{\text{Meas 3}} \times \left(\frac{^{146}\text{Nd}}{^{144}\text{Nd}} \right)_{\text{True}} \times \left(\frac{^{148}\text{Nd}}{^{144}\text{Nd}} \right)_{\text{Dyn 1}}^{\chi} \times \left(\frac{^{148}\text{Nd}}{^{144}\text{Nd}} \right)_{\text{Meas 1}}^{-\chi}$$

$$\text{with } \chi = \frac{\ln \left(\frac{m_{150}}{m_{146}} \right)}{\ln \left(\frac{m_{148}}{m_{144}} \right)}$$

Using (Eq. 9), this can be re-written as follows

$$\begin{aligned} \left(\frac{^{150}\text{Nd}}{^{144}\text{Nd}} \right)_{\text{Dyn 1}} &= \left(\frac{^{150}\text{Nd}}{^{146}\text{Nd}} \right)_{\text{Meas 3}} \times \left(\frac{^{146}\text{Nd}}{^{144}\text{Nd}} \right)_{\text{True}}^{1+\chi+\chi\theta} \times \left(\frac{^{146}\text{Nd}}{^{144}\text{Nd}} \right)_{\text{Meas 1}}^{-\chi\theta} \times \left(\frac{^{148}\text{Nd}}{^{146}\text{Nd}} \right)_{\text{Meas 3}}^{\chi} \\ &\quad \times \left(\frac{^{148}\text{Nd}}{^{144}\text{Nd}} \right)_{\text{Meas 1}}^{-\chi} \quad (\text{Eq. 11}) \\ &= \left(\frac{I^{150}\text{Nd}_3}{I^{146}\text{Nd}_3} \right) \times \left(\frac{^{146}\text{Nd}}{^{144}\text{Nd}} \right)_{\text{True}}^{1+\chi+\chi\theta} \times \left(\frac{I^{146}\text{Nd}_1}{I^{144}\text{Nd}_1} \right)^{-\chi\theta} \times \left(\frac{I^{148}\text{Nd}_3}{I^{146}\text{Nd}_3} \right)^{\chi} \times \left(\frac{I^{148}\text{Nd}_1}{I^{144}\text{Nd}_1} \right)^{-\chi} \\ &\quad \times \left(\frac{C_{\text{H4}} \times G_{\text{H4}}}{C_{\text{H1}} \times G_{\text{H1}}} \right)^{1-\chi} \times \left(\frac{C_{\text{H3}} \times G_{\text{H3}}}{C_{\text{H1}} \times G_{\text{H1}}} \right)^{\chi-\chi\theta} \end{aligned}$$

$\theta = 0.986731$ and $\chi = 0.986693$ using $m_{148} = 147.916899$; $m_{144} = 143.910093$; $m_{150} = 149.920902$ and $m_{146} = 145.9131226$ (AME2012, Wang et al.(2012)). Assuming that faraday cups H4 and H3 degrade similarly relative to H1, this translates into a reduction of 53.7% of the total cup efficiencies and amplifier gains, which is much less efficient than other dynamic ratios but still better than static multicollection. If the ratio $\left(\frac{C_{\text{H4}} \times G_{\text{H4}}}{C_{\text{H1}} \times G_{\text{H1}}} \right)$ degrades faster than $\left(\frac{C_{\text{H3}} \times G_{\text{H3}}}{C_{\text{H1}} \times G_{\text{H1}}} \right)$, then the total reduction of efficiencies and gains is better, for example about 81.9% if $\left(\frac{C_{\text{H4}} \times G_{\text{H4}}}{C_{\text{H1}} \times G_{\text{H1}}} \right)$ varies by 80 ppm and $\left(\frac{C_{\text{H3}} \times G_{\text{H3}}}{C_{\text{H1}} \times G_{\text{H1}}} \right)$ by only 20 ppm.

3. Methods

We evaluated the results of the 4-step method using more than 60 individual runs of the JNdi-1 Nd reference standard (Tanaka et al., 2000) analyzed in multiple sessions over a period of ~1.5 years on 3 different instruments. Additionally, we processed JNdi-1 Nd standards through chemistry following two different Nd separation procedures and analyzed the

reference basalt BHVO-2 to see whether the precision and accuracy calculated from unprocessed standards were applicable to samples.

3.1. Sample digestion and separation of Nd by ion chromatography

The Nd isotopic composition of reference basalt BHVO-2 was analyzed from 10 different dissolutions, all independently processed through column chemistry. We digested about 100 mg of rock powder per Savillex beaker in a mixture of 5 mL of 29N HF + 1 mL of 14N HNO₃ on a hot plate at ~130°C for ~60h. After complete dissolution, and evaporation of the acids, the residues were treated two times with 5 mL of 14N HNO₃ to eliminate fluorides. The samples were then converted to chlorides by adding 3 mL of 6N HCl, twice, drying between applications. The light rare earth elements (LREEs) were separated from the matrix on primary columns (Biorad columns) filled with cation-exchange resin AG50W-X8 (200-400 mesh) by eluting the major elements in 2N HCl, then the LREEs in 6N HCl.

From there, two different separation procedures were used to isolate Nd from the other LREEs. They are shown schematically in Figure 1. The first method, the MLA method, consisted of eluting the LREE with 2-methylactic acid (2-MLA) on long and thin quartz columns (20 cm length x 0.2 cm inner diameter) filled with cation-exchange resin AG50W-X8 (200-400 mesh) in NH₃⁺ form to separate Nd from other LREEs (see Boyet and Carlson, 2005 for further details). The thin geometry of the columns allows a better separation of Nd from other LREEs, but has the inconvenience of significantly slowing down the elution of the acid through the resin. We thus performed the separation under pressure using pure N₂ to accelerate the elution to about 0.05 mL per minute. For each batch of 2-MLA acid, the pH was carefully adjusted to 4.7 and the REE elution profile was recalibrated to ensure good yields and efficient separation of Nd from other LREEs. The MLA separation (Figure 1) was performed twice to ensure the best possible removal of Ce, which interferes with Nd on mass 142. Finally, the Nd cut was further purified on quartz columns (6 cm length x 0.4 cm inner diameter) filled with Ln-Spec resin (50-100 µm) using large volumes of 0.2 N HCl as eluent. This allowed the almost total removal of residual Sm, which interferes with Nd on masses 144, 148 and 150. Overall, the MLA method can be performed in about 4 days. It usually provides a good separation of Nd from other REEs for basaltic matrices and yields relatively low blanks, here < 55 pg of Nd (n = 2). The main inconveniences are (1) the setting-up and calibration of the 2-MLA acid for the 2nd step of the method, (2) the non-reproducibility of the

Nd yields from one sample to another, ranging from 60 to 100% Nd recovery, and (3) the sporadic presence of residual Ce in the Nd cuts for non-basaltic samples.

The second separation procedure, the NaBrO₃ method (Figure 1), uses the oxidation of Ce to Ce⁴⁺ to separate it from the other trivalent LREEs. Details about this technique can be found in Tazoe et al. (2007) and Li et al. (2015). In brief, it involves dissolving the LREE cut from the primary column in a mixture of 10N HNO₃ + 20 mM NaBrO₃ to oxidize Ce(III) to Ce(IV). The concentrated nitric solution containing trivalent LREEs, therefore Nd(III), was then eluted on Ln-Spec resin (50-100 µm) in small columns (1.2 cm length x 0.7 cm inner diameter) while Ce(IV) complexed with the HDEHP of the Ln-Spec resin and remained adsorbed on the resin. This step was performed twice to ensure the total elimination of Ce from the LREE cut. The Nd cut was then processed through a fine Ln-Spec resin (25-50 µm) in quartz columns (6 cm length x 0.4 cm inner diameter) using 0.2N to 0.25N HCl as eluents to recover Nd. We used the finest type of Ln-Spec resin to achieve a better separation of Nd from its neighboring REE, in particular from Pr that is almost not separated from Nd with a coarser resin. Finally, the Nd cut was purified on a small column (2 cm length x 0.8 cm inner diameter) filled with cation resin AG50W-X8 (200-400 mesh) using 2N HNO₃ and 2.5N to 6N HCl to remove the residual traces of Ba and NaBrO₃. Compared to the MLA method, this technique offers the advantage of being easy to set up (no calibration for the 2nd step) and is slightly quicker (i.e. ~ 3.5 days). The method provides good Nd recoveries, generally between 80 and 100%, and a good separation of Nd from Ce and Sm in all types of samples. In this study the NaBrO₃ method yielded slightly higher blanks than the MLA method, perhaps due to the use of NaBrO₃. We measured 125 pg of Nd in the total procedural blank (n=1) but acknowledge that the higher Nd content of the blank could also be due to random contamination (cf. Garçon et al., 2017). The main inconvenience of the NaBrO₃ method is its inability to totally eliminate Pr from the final Nd cut. The use of the finest Ln-Spec resin allows the removal of ~80-90% of Pr which usually produces mean ¹⁴¹Pr/¹⁴⁴Nd ratios < 0.2 during Nd measurements on TIMS. We tested the effects of Pr on Nd isotope analyses by doping a JNdi-1 Nd standard with different amounts of Pr. The results are shown in Appendix A and discussed in Section 4.1.1.d.

Following the chemistry, we systematically analyzed an aliquot of 5% of each processed standard by quadrupole ICP-MS to calculate Nd recoveries and make sure that no residual traces of sample matrix or NaBrO₃ solution were present in the Nd fraction loaded on filaments. Nd recoveries were > 70% for all processed standards (JNdi-1 and BHVO-2).

3.2. Filament loading and TIMS measurements

Neodymium isotope ratios were measured using a double Re filament assembly to enhance the ionization of Nd as a positive metal ion (Nd^+) in the TIMS source. All measurements were performed with the highest quality of Re ribbons (zone-refined Re) that were outgassed for 1 hour at 3.5A under high vacuum and exposed to ambient atmosphere for a few days before loading. Between 750 and 1000 ng of Nd diluted in 1 to 2 μL of 2N HCl was loaded at ~ 0.8 A on one of the two Re filaments, onto small spots, usually ~ 1 mm-wide, to minimize potential mixing effects during measurements (Upadhyay et al., 2008). A small amount (< 0.5 μL) of freshly prepared 1N H_3PO_4 was added to all samples/standards measured at Clermont-Ferrand, France to help stabilize the emission of Nd during measurement. After loading, the filaments were turned to dull red glow for 1 second in air.

The Nd isotopic compositions reported in this study were measured on three different TIMS instruments: the Thermo Scientific™ Triton™ of the Department of Terrestrial Magnetism (DTM), Carnegie Institution for Science (Washington DC, USA), the Thermo Scientific™ Triton™ and Triton Plus™ of the Laboratoire Magmas et Volcans (LMV), Clermont Auvergne University (Clermont-Ferrand, France). The three instruments were equipped with $10^{11}\Omega$ amplifiers on each of the nine-faraday collectors. A typical analytical sequence (one or two barrels) consisted of measuring two JNdi-1 reference standards first to check the proper functioning of the instrument and then one JNdi-1 standard every two or three samples. The physical position of the faraday collectors and the zoom optic parameters were optimized, when necessary, at the beginning of each analytical sequence with the ion beams emitted by a mixed standard of Nd, Sm and Ce. TIMS measurements were started when the source pressure was below 8×10^{-8} mbar, which was usually reached after a night of pumping and the addition of liquid nitrogen to a cold finger directly above the filaments. For each run, the ionization filament current was increased to ~ 4200 mA at a rate of 250-300 mA/minute. At the same time, the evaporation filament current was increased to 1000 mA at a rate of 50 mA/minute. The filament currents were then increased slowly at rates < 50 mA/minute to typical values of 4200-4350 mA for the ionization filament and 1200-1700 mA for the evaporation filament until a stable ^{142}Nd intensity of ~ 5 -6V was reached. The measurements were started after several automatic lens focuses involving all focus plates (Condenser, Left- and Right-Symmetry, X-, Y- and Z-Focus) to ensure the best possible extraction of Nd^+ from the filament to the exit slit of the ion source. Runs consisted of a maximum of 18 blocks of 30 cycles (i.e. 540 cycles, ~ 8 h) with baselines measured for 60 seconds in between each block.

To avoid large and imprecise mass fractionation corrections, measurements were stopped before the end of the 540 cycles when the $^{146}\text{Nd}/^{144}\text{Nd}$ ratio used to correct mass fractionation reached a value of 0.724 or when the ^{145}Nd signal dropped below 0.5V in the axial cup. Each 5 blocks, peaks were centered in the axial cup for each magnet setting and the lenses were automatically refocused using ^{145}Nd in the axial cup (i.e main magnet setting, line 3, Table 1). Calibration of the amplifier gains was performed every 24h. Rotation of the amplifiers between different faraday cups was not employed. To avoid abrupt changes of the filament temperature, the automatic heating routine provided with the TritonTM software was not used. When necessary, the evaporation filament current was increased at a very slow rate of 0.5 to 1 mA/minute during the data acquisition to maintain the stability of the Nd signal during measurement.

3.3. Data processing

Gain, baseline and isobaric interferences from $^{144, 148, 150}\text{Sm}$ and ^{142}Ce were corrected online with the TritonTM software. From the corrected Nd intensities, all static and dynamic ratios were calculated offline using a Matlab routine available on request to the corresponding author. For each run, the routine selects only cycles for which the mean of the $^{146}\text{Nd}/^{144}\text{Nd}$ ratios acquired on lines 1-2-3-4 is lower than 0.724, and for which the ^{145}Nd signal in the axial cup (acquisition line 3) is higher than 0.5 V. For each cycle, the static Nd ratios of each acquisition line are calculated by correcting mass fractionation with the exponential law and a $^{146}\text{Nd}/^{144}\text{Nd}$ ratio of 0.7219. The dynamic Nd ratios are calculated following the equations given in Section 2. The static and dynamic ratios of a run are calculated by averaging the ratios determined at each cycle and by screening for outliers at $\pm 2s$, where s is the standard deviation of the run. The routine generates a table summarizing the mean static and dynamic Nd ratios together with the mean $^{146}\text{Nd}/^{144}\text{Nd}$, $^{140}\text{Ce}/^{144}\text{Nd}$, $^{147}\text{Sm}/^{144}\text{Nd}$ and $^{141}\text{Pr}/^{144}\text{Nd}$ ratios and their 2 s.e., where s.e. is the standard error of the mean (see Table 2 for an example). In Table 2, the means and standard errors of all static ratios (column “All static”) and all dynamic ratios (column “All dynamic”) are calculated by pooling the ratios obtained for each cycle all together, regardless of the acquisition lines from which they are derived; for example, if 540 cycles were acquired, the mean and error of all $^{142}\text{Nd}/^{144}\text{Nd}$ static ratios were calculated from 2160 ratios (4 static ratios per cycle) while the mean and error of all $^{142}\text{Nd}/^{144}\text{Nd}$ dynamic ratios were calculated from 1080 ratios (2 dynamic ratios per cycle). In addition to the summary table, several plots are generated to help the analyst judge the quality

of the run and decide whether a measurement should be accepted or rejected. The different tests and criteria used to accept or reject a run are explained and discussed below in Section 4.1.1.

4. Results and discussion

4.1. The 4-step method: Precision and accuracy of Nd isotope measurements

4.1.1. Criteria to decide whether a run is acceptable

Based on previous work (Andreasen and Sharma, 2009; Sharma and Chen, 2004; Sharma et al., 1996; Roth et al., 2014; Upadhyay et al., 2008; Wielandt and Bizzarro, 2011) and new considerations, we suggest four criteria to help the analyst decide whether a run should be accepted or rejected, in particular when it shows unusual behavior such as reverse fractionation (i.e. when $^{146}\text{Nd}/^{144}\text{Nd}$ ratios decrease through time). In the following evaluation of the results, we systematically rejected the runs that did not satisfy one or more of the four requirements listed below. The total rejection rate is estimated at about 10-15% for the present study. For example, 8 out of 61 runs were rejected for the JNdi-1 reference standards analyzed over ~1.5 years.

4.1.1.a. Mass fractionation following the exponential law

Previous studies have shown that the exponential law is the most accurate law to correct for mass fractionation occurring during Nd isotope measurements by TIMS (Andreasen and Sharma, 2009; Upadhyay et al., 2008). Our measurements of the JNdi-1 reference standard confirm that this is generally the case for the runs showing normal fractionation i.e. $^{146}\text{Nd}/^{144}\text{Nd}$ ratios increasing through the analysis as expected if Nd⁺ is emitted from a single, homogenous domain on the filament. Figure 2a provides an example of such a behavior where the measured $^{142}\text{Nd}/^{144}\text{Nd}$ and $^{146}\text{Nd}/^{144}\text{Nd}$ ratios oscillate around the trend expected for a mass-bias that follows the exponential law (red line in Figure 2a). Runs may have short periods of time during which mass fractionation slightly departs from the exponential law and follows either the Rayleigh or the Power law. Since these periods of time are sporadic and usually very short compared to the total length of a run, there is, in our opinion, no obvious reason to correct the mass-bias by a law other than the exponential law. In addition, dynamic ratios corrected with the power law do not provide a more precise result compared to those corrected with exponential law.

In some runs, however, the relationship between measured $^{142}\text{Nd}/^{144}\text{Nd}$ and $^{146}\text{Nd}/^{144}\text{Nd}$ ratios shows large variations inconsistent with the trends predicted by any of the common

fractionation laws for very long periods of time, i.e. for several measurement blocks. This usually happens when the fractionation is reverse for a significant part of the run (i.e. $^{146}\text{Nd}/^{144}\text{Nd}$ ratios decrease through the analysis) or switches from normal to reverse several times during the run. An example of the latter case is shown in Figures 2b-d. Reverse fractionation very likely indicates evaporation and mixing of Nd from variably fractionated domains on the filament (Andreasen and Sharma, 2009; Hart and Zindler, 1989; Russell et al., 1978; Sharma and Chen, 2004; Upadhyay et al., 2008). The mass fractionation of the Nd+ beam emitted by each domain individually follows the exponential law, but the Nd+ beam coming from the different domains that is finally extracted from the source and collected in the faraday cups follows linear mixing trends between the different domains. The amplitude of this effect cannot be predicted, and thus corrected, since it depends, at any given time, on the number of domains emitting Nd+, and on the amount and fractionation stage of Nd+ emitted by each domain. Although we loaded the samples/standards onto very small spots to minimize the formation of clumps, domain mixing on the filament is likely the reason why some runs exhibit large departures from common fractionation laws as shown in Figure 2b. Upadhyay et al.(2008) and Andreasen and Sharma (2009) demonstrated that using the exponential law to correct for mass fractionation when Nd is emitted from multiple domains can significantly bias $^{142}\text{Nd}/^{144}\text{Nd}$, $^{148}\text{Nd}/^{144}\text{Nd}$, and $^{150}\text{Nd}/^{144}\text{Nd}$ ratios towards higher than true values and $^{145}\text{Nd}/^{144}\text{Nd}$ towards lower values. Importantly, Andreasen and Sharma (2009) showed that data collected during, after, or before reverse fractionation are all affected by domain mixing effects. Therefore, to ensure the best possible measurement precision and accuracy, we rejected runs showing large and sporadic departures from the common fractionation laws, which was the case for 3 out of 61 runs in the present study. As shown in Figure 2b and d, this first criterion generally removes runs that show long or repetitive periods of reverse fractionation.

4.1.1.b. Poisson noise and minimum number of ratios to measure

Different sources of error can affect the measurement of dynamic Nd isotope ratios. Systematic errors, such as those induced by domain mixing on the filament, are difficult to predict and thus to correct. Random errors due to counting statistics (i.e. Poisson noise) or instrument electronic stability (mainly Johnson-Nyquist noise) are easier to predict, and their level can generally be minimized by optimizing measurement conditions. Figure 3a shows how the standard deviation of the combined dynamic $^{142}\text{Nd}/^{144}\text{Nd}$ ratios varies as a function of the mean ^{142}Nd beam intensity of the runs. The strong relationship observed between

standard deviation and ion beam intensity, independent of the instrument and the analytical sequence, suggests that the main factor limiting the internal precision is ion counting statistics (i.e. Poisson noise). To verify this hypothesis, we calculated the predicted Poisson noise $\sigma_P(U_{142})$ for different ^{142}Nd beam intensities as follows:

$$\sigma_P(U_{142}) = \sqrt{\frac{e \times R \times U_{142}}{t_s}} \quad (\text{Eq. 12})$$

where e is the elementary charge in Joules, R the feedback resistor in Ohms (in our case, $R = 10^{11} \Omega$), U_{142} is the mean ^{142}Nd beam of the run in Volts, t_s is the integration time in seconds (here $t_s = 8.389\text{s} \times 2$ since we calculate 2 independent dynamic $^{142}\text{Nd}/^{144}\text{Nd}$ ratios per cycle). Using $^{142}\text{Nd}/^{144}\text{Nd} = 1.141835$, and $^{146}\text{Nd}/^{144}\text{Nd} = 0.7219$ as an average composition for the JNdi-1 standard, we estimate the Poisson noise on ^{144}Nd and ^{146}Nd intensities, propagate the errors on the measured $^{142}\text{Nd}/^{144}\text{Nd}$ and $^{146}\text{Nd}/^{144}\text{Nd}$ ratios, and then on the dynamic $^{142}\text{Nd}/^{144}\text{Nd}$ ratios using Monte-Carlo simulations. The result of this calculation, shown by a dashed line in Figure 3a, well fits the observed trend between ^{142}Nd beam intensity and standard deviation (1s). The slight shift of the data to the right of the modeled curve corresponds to an unknown additional imprecision of 0.1 to 0.2 ppm on the final standard error of the runs, which can be considered negligible. This confirms that counting statistics are the main factor limiting the internal precision of the measurements. Note that the contribution of amplifier noise level (i.e. Johnson-Nyquist noise) for the $10^{11} \Omega$ feedback resistor to isotope ratio precision is negligible compared to the Poisson noise. The amplifier noise level ranges from a maximum of 3% of the Poisson noise at 1V to about 0.5% at 12V, as previously discussed by Wielandt and Bizzarro (2011).

Since the standard deviation of a run is predictable and controlled by beam intensity, one can define the minimum integration time (or minimum number of ratios) needed so that the mean of the dynamic $^{142}\text{Nd}/^{144}\text{Nd}$ ratios be determined at $\pm \delta$ ppm with a 95% confidence level at any given intensity. Assuming that the distribution of $^{142}\text{Nd}/^{144}\text{Nd}$ ratios is normal, this involves calculation of the minimum number of ratios, N , needed to obtain a standard error $\frac{s}{\sqrt{N}} \leq \frac{\delta}{z_c}$, where z_c is the critical value of the standard normal distribution corresponding to the desired level of confidence c ($z_c = 1.96$ for a 95% confidence level), σ is the standard deviation of the dynamic $^{142}\text{Nd}/^{144}\text{Nd}$ ratios (i.e. $\left(\frac{^{142}\text{Nd}}{^{144}\text{Nd}}\right)_{\text{Dyn 1}}$ and $\left(\frac{^{142}\text{Nd}}{^{144}\text{Nd}}\right)_{\text{Dyn 2}}$ pooled together) and δ is the margin of error. Hence,

$$N \geq \left(\frac{Z_c}{\delta}\right)^2 \times s^2 \quad (\text{Eq. 13})$$

Knowing the relationship between standard deviation and ^{142}Nd beam intensity (cf. Figure 3a), defines the minimum number of ratios to measure to establish a mean dynamic $^{142}\text{Nd}/^{144}\text{Nd}$ ratio at ± 3 , and ± 5 ppm with a 95% confidence level as a function of the mean ^{142}Nd intensity of a run (cf. Figure 3b). If the mean ^{142}Nd beam intensity of a run is 3V, one should measure at least 390 ratios to ensure the detection of a 5 ppm ^{142}Nd anomaly with 95% confidence, and at least 1080 ratios if the aim is to detect a 3 ppm anomaly with 95% confidence. In the following evaluation of the results, we systematically rejected runs for which the number of measured ratios was too low to detect a 5-ppm anomaly with 95% confidence. This criterion led to the rejection of 3 out of 61 runs for the unprocessed JNdi-1 standards.

4.1.1.c. Stable cumulative mean for dynamic Nd isotope ratios

Measuring a large number of ratios is important to establish a mean value with a low internal error at a high confidence level. For this statement to be valid, however, requires that the mean of the measured ratios converges to the true value of the sample/standard by the end of the run. This implies that the cumulative mean of the measured ratios should reach a plateau before the end of the run when plotted against measurement cycle. In the run illustrated in figure 4a, the dynamic $^{142}\text{Nd}/^{144}\text{Nd}$ ratios converge to the mean value of the run within ± 1.5 ppm (2 s.e.) after only 120 cycles and stay within that error limit for the remainder of the run. While most runs exhibit a similar behavior, some runs never converged to a plateau, as shown in Figure 4b. This is problematic because in such a run, the final calculated mean value depends on the number of measured cycles. In Figure 4b, if the run was stopped after about 300 cycles, the final calculated dynamic $^{142}\text{Nd}/^{144}\text{Nd}$ ratio is about 5 ppm lower than the value obtained after 540 cycles, a bias that is well above the final internal error reported for the run i.e. ± 1.5 ppm (2 s.e.). This behavior may again be related to domain mixing effects as the formation of variably fractionated domains on the filament after ~ 300 cycles would be compatible with the sudden increase of the mean dynamic $^{142}\text{Nd}/^{144}\text{Nd}$ value. This is also supported by the evolution of $^{146}\text{Nd}/^{144}\text{Nd}$ ratios through time, changing from a smooth increasing trend to a stable evolution after ~ 300 cycles (cf. Figure 4d). In the following, we developed a criterion that allows the identification of ‘unstable mean values’. We arbitrarily defined an unstable mean as a mean value that varies beyond ± 2 times the final standard error for the last quarter of the run. Runs yielding an unstable mean for the combined dynamic

$^{142}\text{Nd}/^{144}\text{Nd}$ ratios (2 runs out of 61 for the unprocessed JNdi-1 Nd standards) were rejected and not taken into account in the evaluation of the method results. The ‘unstable mean criterion’ can be more generally applied to all dynamic ratios.

4.1.1.d. Maximum isobaric interferences

Cerium and Sm are the most critical potential interfering elements as they both have isobars with Nd. Cerium interferes on mass 142, and hence affects the measurement of $^{142}\text{Nd}/^{144}\text{Nd}$ ratios, while Sm interferes on masses 144, 148, and 150, and hence impacts all Nd isotope ratios through its contribution to the normalizing isotope ^{144}Nd . When residual Sm and/or Ce are present in the samples, isobaric interferences are generally corrected online using the measured ^{147}Sm and ^{140}Ce beams and assuming constant values for the $^{142}\text{Ce}/^{140}\text{Ce}$, $^{144}\text{Sm}/^{147}\text{Sm}$, $^{148}\text{Sm}/^{147}\text{Sm}$, and $^{150}\text{Sm}/^{147}\text{Sm}$ ratios. In this correction, the most important source of error arises from the fact that mass fractionation of the interfering element is not known, hence not taken into account for Ce and Sm isotope ratios. Since each element has its own fractionation trend through time on TIMS, using the fractionation factor of Nd to correct the Sm and Ce ratios, as commonly done on MC-ICP-MS, may introduce additional errors instead of improving the isobaric correction. To evaluate the effects of such an approximation, we propagated the errors arising from imprecise isobaric interference corrections on all Nd isotope ratios using Monte-Carlo simulations (Figure 5). The calculations were performed for different amounts of interfering Ce and Sm assuming that their isotope ratios were highly fractionated during measurement, that is with fractionation factors, f , varying between -1 and +1. This roughly corresponds to a $^{140}\text{Ce}/^{142}\text{Ce}$ ratio ranging from 0.123 to 0.128 and a $^{144}\text{Sm}/^{147}\text{Sm}$ ratio from 0.201 and 0.209 using atomic masses of Wang et al. (2012), and $^{140}\text{Ce}/^{142}\text{Ce} = 0.12565$ and $^{144}\text{Sm}/^{147}\text{Sm} = 0.20506$ as ‘true’ values (Chang et al., 1995; 2002). This extreme mass fractionation scenario allowed us to calculate the maximum amounts of Ce and Sm that can be tolerated in a sample to ensure that the errors induced by imprecise isobaric interference corrections remain lower than 5 ppm on all dynamic Nd isotope ratios. Our results indicate that ignoring the mass fractionation of the $^{140}\text{Ce}/^{142}\text{Ce}$ ratio can lead to errors > 5 ppm on dynamic $^{142}\text{Nd}/^{144}\text{Nd}$ ratios as soon as the $^{140}\text{Ce}/^{146}\text{Nd}$ ratio is higher than $\sim 1.6 \times 10^{-3}$ (Figure 5a). For Sm interference corrections, the situation is slightly more complex since the errors propagate to all Nd isotope ratios, but to different degrees. According to the simulations, the dynamic $^{150}\text{Nd}/^{144}\text{Nd}$ ratio is the most affected by imprecise Sm isobaric interference corrections (Figure 5b). Errors on the determination of this ratio become higher than 5 ppm when the $^{147}\text{Sm}/^{146}\text{Nd}$ ratio of the

sample reaches a value of $\sim 1.2 \times 10^{-4}$. Note that the tolerance is higher for the dynamic $^{142}\text{Nd}/^{144}\text{Nd}$ ratio since the propagated errors remain < 5 ppm as long as the $^{147}\text{Sm}/^{146}\text{Nd}$ ratio is below $\sim 4.3 \times 10^{-4}$. Therefore, unless the collector configuration allows for the determination of the precise fractionation stage of Ce and Sm during Nd analyses, we recommend that runs having mean $^{140}\text{Ce}/^{146}\text{Nd}$ and $^{147}\text{Sm}/^{146}\text{Nd}$ ratios $> 1.6 \times 10^{-3}$ and $> 1.2 \times 10^{-4}$, respectively, be systematically rejected. In this study, the maximum mean $^{140}\text{Ce}/^{146}\text{Nd}$ and $^{147}\text{Sm}/^{146}\text{Nd}$ ratios ever measured for a run were well below these limits i.e. 9.8×10^{-5} and 4.8×10^{-6} , respectively (cf. Appendix A, B, C). Interferences of this magnitude also introduce the concern that such small signals are not easily quantified with faraday detectors equipped with 10^{11} Ohm resistors. For example, for a ^{142}Nd signal of 2V, a $^{147}\text{Sm}/^{146}\text{Nd}$ ratio of 5×10^{-6} corresponds to a ^{147}Sm signal of only 6 μV , which is indistinguishable from the noise in a faraday cup using amplifiers with a 10^{11} Ohm feedback resistor. Quantifying interferences at this scale thus requires either higher ohmage feedback resistors for the faraday cup amplifier used to detect the interference, or the use of ion multipliers, with the inherent difficulty of gain calibration between the detectors.

Another potential problem that may lead to imprecision in the determination of dynamic Nd isotope ratios is the presence of Pr. Praseodymium concentrations are 3-5 times lower than Nd concentrations in natural samples but the NaBrO_3 method fails to effectively remove this element from the Nd fraction (cf. Section 3.1). The most likely potential isobaric interference during Nd analysis by TIMS is by ^{141}PrH on ^{142}Nd . However, large Pr ion beams could also produce a peak tailing effect on ^{142}Nd and thus bias $^{142}\text{Nd}/^{144}\text{Nd}$ ratios. To test whether these effects were important, we doped 3 JNdi-1 Nd standards with variable amounts of Pr to obtain solution that produced mean $^{141}\text{Pr}/^{146}\text{Nd}$ ratios from ~ 0.3 to 1.3. Results are shown in Appendix A together with un-doped JNdi-1 Nd standards. No systematic bias was observed on dynamic Nd isotope ratios as a function of Pr amounts; hence we conclude that the residual presence of Pr in samples is not problematic for the determination of precise Nd isotope ratios by TIMS, at least for samples with $^{141}\text{Pr}/^{146}\text{Nd}$ ratios $< \sim 1.3$.

4.1.2. Fractionation rate and drift correction

Dynamic measurements theoretically reduce most of the imprecision arising from collector inefficiencies and amplifier gains. The drawback, however, is that the ratios used for dynamic calculations are not measured at the same time, and hence can potentially record different stages of fractionation. Roth et al. (2014) suggested that, if Nd fractionates quickly, the lapse of time between the acquisition of the $^{146}\text{Nd}/^{144}\text{Nd}$ and the $^{142}\text{Nd}/^{144}\text{Nd}$ ratios could be enough

to induce large biases, up to 8 ppm, on dynamic $^{142}\text{Nd}/^{144}\text{Nd}$ ratios. The bias can be either positive or negative depending on the order in which the ratios used for dynamic calculations are acquired. For example, measuring the $^{146}\text{Nd}/^{144}\text{Nd}$ ratio before the $^{142}\text{Nd}/^{144}\text{Nd}$, as done by Roth et al. (2014) and Upadhyay et al. (2009), may bias the dynamic $^{142}\text{Nd}/^{144}\text{Nd}$ ratios towards lower than true values for high fractionation rate. Conversely, measuring the $^{142}\text{Nd}/^{144}\text{Nd}$ ratio first, as in our collector configuration (Table 1) may bias dynamic $^{142}\text{Nd}/^{144}\text{Nd}$ ratios towards higher than true values. The longer is the time gap and the higher is the fractionation rate, the larger will be the effect on dynamic Nd isotope ratios. In their study, Roth et al. (2014) calculated a threshold limit for the average fractionation rate of a run over which they estimated that the bias on dynamic $^{142}\text{Nd}/^{144}\text{Nd}$ ratios should be higher than 5 ppm. They suggested that any run having an average fractionation rate higher than the threshold limit should be treated as suspicious.

Here, we go further and suggest a method to systematically correct for the drift of Nd isotope ratios in between acquisition lines whatever the fractionation rate. The method consists of determining the local fractionation trend of Nd isotope ratios by fitting a least-square regression line through several consecutive measurements of the same ratio. Using the equation of the fitted line, the isotope ratios of interest can then be recalculated at any time t . An illustration of the method is shown in Figure 6 for the $^{146}\text{Nd}/^{144}\text{Nd}$ ratio acquired on line 3. This ratio is used, together with the $^{142}\text{Nd}/^{144}\text{Nd}$ ratio from acquisition line 1, to calculate the first dynamic $^{142}\text{Nd}/^{144}\text{Nd}$ ratio (cf. Eq. 2). To correct for the drift of $^{146}\text{Nd}/^{144}\text{Nd}$ ratios between lines 1 and 3, we approximated, for each cycle N , the local fractionation trend of $^{146}\text{Nd}/^{144}\text{Nd}$ ratios as linear over 11 consecutive cycles, from $N-5$ to $N+5$ (see inset of Figure 6). The number of cycles used to interpolate the fractionation trend should be large enough to minimize noise contribution, but small enough so that the local variation of $^{146}\text{Nd}/^{144}\text{Nd}$ ratios through time can always be approximated as linear. We found that 11 consecutive measurements was the best compromise to describe the variation of all Nd isotope ratios through time, regardless of the fractionation rate and the signal/noise ratio. Note that determining the equations of the local fractionation trends as a function of time t (and not as a function of cycles N) allows to properly take into account fractionation during blanking time, lens refocusing and peak centering when no measurement is performed. The drift-correction assumes a linear fractionation over 11 consecutive measurements, and hence requires that the evolution of Nd isotope ratios be as smooth as possible. Abrupt changes or step-variations such as those caused by the automatic heating function of the Triton™ software at the end of

each block, or accompanying changes in source focus, likely will make the correction imprecise.

Assuming that the data were collected with collector configuration 1 (Table 1), we used the equation of the fitted fractionation line to recalculate the value of the $^{146}\text{Nd}/^{144}\text{Nd}$ ratio as if it was measured two lines before (i.e. 2×8.39 seconds (integration time) + 2×3 seconds (idle time) = 22.78 seconds earlier), at the time when the $^{142}\text{Nd}/^{144}\text{Nd}$ ratio was acquired. This drift-corrected $^{146}\text{Nd}/^{144}\text{Nd}$ ratio was then used to calculate the drift-corrected dynamic $^{142}\text{Nd}/^{144}\text{Nd}$ ratio following Eq. (2). The same correction is applied to the second dynamic $^{142}\text{Nd}/^{144}\text{Nd}$ ratio and to the dynamic $^{148}\text{Nd}/^{144}\text{Nd}$ ratios by monitoring the fractionation trends of $^{146}\text{Nd}/^{144}\text{Nd}$ ratios measured on different acquisition lines and by recalculating their values at the desired time. Correcting the dynamic $^{143}\text{Nd}/^{144}\text{Nd}$, $^{145}\text{Nd}/^{144}\text{Nd}$, and $^{150}\text{Nd}/^{144}\text{Nd}$ ratios for drift is a bit trickier as they use more than two measured ratios, sometimes from three different acquisition lines (cf. Eq. 4-5, Eq. 6-8 and Eq. 11). Hence, one needs to interpolate the variations of $^{143}\text{Nd}/^{144}\text{Nd}$, $^{145}\text{Nd}/^{144}\text{Nd}$ and $^{148}\text{Nd}/^{144}\text{Nd}$ through time, in addition to those of $^{146}\text{Nd}/^{144}\text{Nd}$, and recalculate their values at the same time t . In the following, drift-corrected $^{143}\text{Nd}/^{144}\text{Nd}_{\text{Dyn } 1}$ and $^{145}\text{Nd}/^{144}\text{Nd}_{\text{Dyn } 1}$ were determined with ratios brought back to the acquisition time of line 2, drift-corrected $^{143}\text{Nd}/^{144}\text{Nd}_{\text{Dyn } 2}$, $^{145}\text{Nd}/^{144}\text{Nd}_{\text{Dyn } 2}$, and $^{150}\text{Nd}/^{144}\text{Nd}_{\text{Dyn } 1}$ with ratios recalculated at the acquisition time of line 3, and drift-corrected $^{145}\text{Nd}/^{144}\text{Nd}_{\text{Dyn } 3}$ with ratios recalculated to the acquisition time of line 4. The effects of the drift-correction on all dynamic Nd isotope ratios are discussed in the following section of the manuscript.

4.1.3. Comparison of the different ratios acquired during a run

4.1.3.a. Static vs. dynamic Nd isotope ratios

Figure 7 compares static and dynamic Nd isotope ratios of JNdi-1 Nd standards acquired over a period of ~1.5 years on the TritonTM from Carnegie, and the TritonTM and Triton PlusTM from LMV. The measured ratios and a compilation of the means and standard deviations are provided in Appendix A and Table 3, respectively. The data confirm that, over long periods of time, dynamic Nd isotope measurements yield better long-term reproducibility and more accurate results than static measurements due to the removal of the component of scatter arising from collector inefficiencies and amplifier gains (cf. Section 2). Average static ratios have external precisions ~1.5 to 3 times worse than dynamic ratios, except for $^{145}\text{Nd}/^{144}\text{Nd}$ ratios (Table 3). The latter exhibit large variations on individual static ratios but a surprisingly good external precision on the average of all static ratios that can be mathematically explained

by the fortunate cancellation of several cup efficiencies and amplifier gains when averaging the four static $^{145}\text{Nd}/^{144}\text{Nd}$ ratios. As previously noticed by several authors (Carlson, 2014; Fukai et al., 2017; O'Neil et al., 2008), the change of the whole set of faraday cups, including the axial cup, in the LMV TritonTM (green and blue squares in Figure 7) resulted in a large shift, up to 100 ppm, of the static ratios. Following this shift, the set of collectors of the LMV TritonTM may have slowly deteriorated and caused the static ratios to deviate between April 2016 and January 2017 (cf. blue squares in Figure 7). The imprecision and inaccuracy of static ratios over long periods of time can also be highlighted on binary plots, as illustrated in Figure 8 where static $^{142}\text{Nd}/^{144}\text{Nd}$ ratios from acquisition line 1 (i.e. $^{142}\text{Nd}/^{144}\text{Nd}_{\text{Static } 1}$) are reported as a function $^{148}\text{Nd}/^{144}\text{Nd}_{\text{Static } 3}$. Equations for exponential mass-fractionation correction show that the $^{142}\text{Nd}/^{144}\text{Nd}_{\text{Static } 1}$ and $^{148}\text{Nd}/^{144}\text{Nd}_{\text{Static } 3}$ scale to roughly the same combination of collector efficiencies and amplifier gains, that is to $\sim \frac{C_{L1} \times G_{L1}}{C_{H1}^2 \times G_{H1}^2} \times C_{H3} \times G_{H3}$.

In Figure 8, the deterioration of these faraday cups translate into the strong positive co-variation of $^{142}\text{Nd}/^{144}\text{Nd}_{\text{Static } 1}$ and $^{148}\text{Nd}/^{144}\text{Nd}_{\text{Static } 3}$ measured in JNdi-1 Nd standards on the LMV TritonTM. Deviations of static ratios due to cup deterioration are observed at the scale of one analytical session i.e. within two weeks of measurements when cups are relatively old (cf. green squares in Figure 8), which reinforces the need to determine all Nd isotope ratios dynamically to ensure the best possible accuracy. The number of data acquired on the Carnegie TritonTM might not be enough to precisely determine the trend resulting from cup deterioration, but it seems that the instrument use may have caused the static ratios to deviate in the opposite way compared to the LMV TritonTM data. This shows that cup deterioration trends strongly vary as a function of the instrument use, hence are likely not predictable unless the instrument is dedicated to the measurement of just one isotopic system.

Figure 7 and Table 3 show clearly that dynamic acquisition of the ratios significantly minimized the effect of cup deterioration through time. Nevertheless, small shifts persist for a few dynamic ratios after the change of the faraday cups and through time for the data acquired with the LMV TritonTM. This likely reflects the failure of dynamic measurements to completely cancel out the effects of cup efficiencies and amplifier gains as demonstrated in Section 2. Dynamic measurements also do not erase differences measured between instruments, which can be linked to other TIMS features such as the position of the magnet and the cup inserts, the tuning of the electrostatic and magnetic optic system, etc. We note that the measurements performed on the older generation of TIMS instrument (i.e. TritonsTM from Carnegie and LMV) are more consistent with each other than measurements performed

on the newer generation of Triton™ (i.e. Triton Plus™ from LMV). This means that absolute ratios should not be compared between instruments when investigating variations at the 5 to 10 ppm levels. These residual differences can of course be suppressed by looking at relative ratios instead of absolute values. Given that the sources of the residual differences are related to the instrument itself and to the deterioration stage of the faraday cups, we divided our JNdi-1 dataset into five groups (cf. Table 4) to calculate the relative variability in isotope ratios (μ values) shown in Figure 9. A group gathers data collected on the same instrument and over a period of 4 months maximum.

4.1.3.b. Uncorrected vs. drift-corrected dynamic Nd isotope ratios

The effects of the drift-correction on dynamic Nd isotope ratios can be evaluated by comparing absolute ratios as in Tables 3 and 4, or relative μ values as shown in Figures 9 and 10. Figure 9a confirms the expected relationship between the rate at which Nd fractionates during a run and the resulting dynamic $^{142}\text{Nd}/^{144}\text{Nd}$ ratios. The deviation of the compositions towards higher than true values (i.e. $\mu_{142} > 0$) for high fractionation rates is consistent with our cup configurations as explained in Section 4.1.2. More importantly, we note that processing the standards through chemistry results in higher fractionation rates, and hence significantly increases the risk of shifting the dynamic ratios towards high μ_{142} values. Such behavior is particularly obvious when comparing unprocessed JNdi-1 Nd standards to those measured during the same analytical sequence, but processed through different chemistries following the MLA or NaBrO₃ methods (cf. pink diamonds in Figure 9a). Standards having the highest fractionation rates also have the highest ^{142}Nd excesses, up to +19 ppm according to our measurements. This suggests that samples may be more likely affected by drift effects than unprocessed JNdi-1 standards generally used to evaluate the accuracy and the precision of Nd measurements. This may be due to the presence of organic residues from the resin and/or to the lower amount of Nd analyzed in samples compared to unprocessed JNdi-1 standards. Using unprocessed JNdi-1 standards to evaluate the quality of Nd isotope analyses may lead to an underestimation of the accuracy and precision of the dynamic compositions of the samples, unless drift effects are accurately corrected. In Figure 9b, the drift-correction efficiently eliminates the large positive μ_{142} biases of standards having high mean fractionation rates, up to 0.6 ppm/s, and does not over-correct standards having mean fractionation rates close to zero. Similar efficiencies were observed for other dynamic Nd isotope ratios (see Appendix A and B, Tables 3 and 4), suggesting that the drift-correction enhances the accuracy of the measurements. The drift-correction also generally improves the

external precision of all dynamic Nd isotope ratios; the best improvements being noticed for dynamic $^{142}\text{Nd}/^{144}\text{Nd}$ and $^{143}\text{Nd}/^{144}\text{Nd}$ ratios as shown in Tables 3 and 4 and in Figure 10. With the drift-correction, providing that the measurements respect the 4 criteria discussed above, one can reliably ensure a precision of 2-5 ppm (2s) for both relative and absolute dynamic $^{142}\text{Nd}/^{144}\text{Nd}$ ratios. Under the same conditions, the method systematically returns precisions of 1-3 ppm (2s) for dynamic $^{143}\text{Nd}/^{144}\text{Nd}$ and $^{145}\text{Nd}/^{144}\text{Nd}$ ratios, 5-10 ppm (2s) for dynamic $^{148}\text{Nd}/^{144}\text{Nd}$ ratios and 15-23 ppm (2s) for dynamic $^{150}\text{Nd}/^{144}\text{Nd}$ ratios. The poorer $^{150}\text{Nd}/^{144}\text{Nd}$ precision is due to cup configurations that allow the determination of only one dynamic ratio per cycle while at least two ratios can be determined for the other Nd isotopic compositions (see equations in Section 2), but probably also to the fact that ^{150}Nd is collected in an outer cup. We acknowledge that the $^{150}\text{Nd}/^{144}\text{Nd}$ ratio is often critical for cosmochemical studies but it is difficult to obtain a good precision and accuracy for both the lightest isotope (^{142}Nd) and the heaviest one (^{150}Nd) with the same cup configuration. In this study, we chose to focus on a cup configuration that allowed the best possible precision and accuracy for the $^{142}\text{Nd}/^{144}\text{Nd}$ ratio. If the focus is to obtain a better precision on the $^{150}\text{Nd}/^{144}\text{Nd}$ ratio, then the cup configuration should be changed to get the ^{150}Nd beam in a more central position so that several $^{150}\text{Nd}/^{144}\text{Nd}$ dynamic ratios could be calculated per cycle. Overall, the precisions returned by the 4-step method are limited by counting statistics (cf. Figure 3) and could theoretically be improved by increasing the average Nd intensity or the integration time. Such precisions are either similar or better than those reported by previous studies (cf. Andreasen and Sharma, 2006; Bennett et al., 2007; Boyet and Carlson, 2005; Brandon et al., 2009; Morino et al., 2017; O'Neil et al., 2008; Rizo et al., 2012; Roth et al., 2014). However, since the 4-step method is the only one to 1) make possible the acquisition of all Nd isotope ratios dynamically and 2) to integrate a systematic drift-correction in between the acquisition lines, it should theoretically provide the most accurate values. Therefore, we propose that the values reported in Table 3 (dynamic drift-corrected) be used as reference for the absolute Nd isotopic composition of the JNdi-1 reference standard in further studies.

To see whether the drift effects could be reduced on dynamic $^{142}\text{Nd}/^{144}\text{Nd}$ ratios, we measured a few standards (Jan-2017 sequence, see Appendix A) with another collector configuration in which the time gap between the acquisition of $^{146}\text{Nd}/^{144}\text{Nd}$ and $^{142}\text{Nd}/^{144}\text{Nd}$ ratios was shorter by a factor of two (cf. Configuration 2 in Table 1). The isotope beams are collected in the same collectors as in Configuration 1; the only difference is the order in which the acquisition lines are performed. In theory, such a configuration should reduce the amplitude of the drift

effects by a factor of two on dynamic $^{142}\text{Nd}/^{144}\text{Nd}$ ratios compared to Configuration 1. Configuration 2 should also minimize the drift effects on dynamic $^{148}\text{Nd}/^{144}\text{Nd}$ and $^{150}\text{Nd}/^{144}\text{Nd}$ ratios and increase them on $^{143}\text{Nd}/^{144}\text{Nd}$ and $^{145}\text{Nd}/^{144}\text{Nd}$ ratios. However, the expected precision improvement is not obvious when comparing the JNdi-1 data collected with Configuration 2 to those collected with Configuration 1 (Table 4). This could be because the mean fractionation rates of the tested standards were not high enough to significantly shift the ratios (Figure 9). Given the efficacy of the drift-correction, we think that the two collector configurations are equivalent and result in similar accuracy and precision on all Nd dynamic ratios. One or the other can therefore be used provided that the drift-correction is systematically integrated in the calculation of dynamic ratios.

4.2. Fractionation caused by chromatographic separation

4.2.1. JNdi-1 Nd standards processed through chemistry

The Nd isotopic composition of the JNdi-1 standards processed through ion chromatography following the NaBrO_3 and MLA methods (cf. Section 3.1. and Figure 1 for a description of the two procedures) are shown in Figure 11. As mentioned earlier, the processing of the standards through chemistry caused more rapid fractionation of Nd on the filaments and was responsible for larger inaccuracy and imprecision on drift-uncorrected Nd dynamic ratios. The NaBrO_3 method in particular seems to generate higher deviations and scatter than the MLA method. The reason for this behavior is unclear. Perhaps the NaBrO_3 method results in higher amounts of organic compounds from the Ln-spec resins or residual NaBrO_3 that somehow inhibit the ionization of Nd and result in higher fractionation rates. Applying the drift correction allowed the complete removal of the drift effects and yielded better external precision on almost all dynamic Nd isotope ratios (Figure 11). Overall, precisions for drift-corrected ratios are similar to those reported for unprocessed JNdi-1 standards (Figure 10).

In Figure 11, the drift-corrected Nd isotopic compositions of JNdi-1 Nd standards treated with the NaBrO_3 method show residual positive μ_{143} and μ_{145} deviations together with negative μ_{148} and μ_{150} . The negative μ_{150} is not an artifact of the drift-correction since the deviation is also observed for static measurements (see Appendix D). The residual deviations are not resolvable outside 2 standard deviations but two sample t-tests result in p-values of 0.00003, 0.000006, 0.024, and 0.000002 for drift-corrected dynamic μ_{143} , μ_{145} , μ_{148} and μ_{150} , respectively, showing that the population means of JNdi-1 standards processed through the NaBrO_3 method are likely different from those of unprocessed standards and standards processed through the MLA method. The same test yields a p-value of 0.33 for μ_{142} indicating

that the data populations likely share the same mean, hence are statistically not different. This suggests that the NaBrO₃ procedure may slightly fractionate all Nd isotope ratios except for ¹⁴²Nd/¹⁴⁴Nd. Previous studies have suggested that the nuclear field shift effect could be responsible for isotope fractionation during chemical exchange reactions of heavy elements (Cook and Schönbächler, 2016; Fujii et al., 2009; Yang and Liu, 2016), including Nd isotopes during solvent extraction (Fujii et al., 2000) and chromatographic separation on cation-exchange resin (Saji et al., 2016; Wakaki and Tanaka, 2012). The nuclear field shift effect is a mass-independent isotope fractionation directly related to the fact that isotopes do not have the same number of neutrons and hence do not share the exact same shape and size of atomic nucleus. These nuclear differences are responsible for differences in the zero-point energy levels (i.e. ground-state energy) of the electronic systems that cause the isotopes to behave differently during chemical exchange reactions (see Fujii et al., 2009 and Yang and Liu, 2016 for a complete review of the process). In Figure 12, we modeled the theoretical effect of the nuclear field shift for Nd isotopes. The shift μ_i can be predicted for each Nd isotope ratio from the equation derived by Fujii et al. (2006) for a mass-fractionation following the exponential law and normalized to the ¹⁴⁶Nd/¹⁴⁴Nd ratio:

$$\mu_i \text{ (ppm)} = \left[\left(\langle r^2 \rangle_i - \langle r^2 \rangle_{^{144}\text{Nd}} \right) - \frac{m_{^{146}\text{Nd}} \times (m_i - m_{^{144}\text{Nd}})}{m_i \times (m_{^{146}\text{Nd}} - m_{^{144}\text{Nd}})} \times \left(\langle r^2 \rangle_{^{146}\text{Nd}} - \langle r^2 \rangle_{^{144}\text{Nd}} \right) \right] \times \alpha$$

where $\langle r^2 \rangle_i$ is the mean-squared nuclear charge radii of isotope *i* (Heilig and Fricke, 2004), m_i its atomic mass (AME2012, Wang et al.(2012)), and α a scaling factor for the amplitude of the effect. Note that the equation simply describes the relative variation of an isotope *i* relative to ¹⁴⁴Nd; the amplitude and sign of the effect are adjusted with the parameter alpha. By definition, $\mu_{^{146}\text{Nd}}$ and $\mu_{^{144}\text{Nd}}$ equal zero and are not represented in Figure 12. The fractionation pattern of JNdi-1 standards processed through chemistry following the NaBrO₃ method is entirely consistent with fractionation caused by the nuclear field shift effect. Theory predicts small excesses in $\mu_{^{143}\text{Nd}}$ and $\mu_{^{145}\text{Nd}}$ and large deficits in $\mu_{^{148}\text{Nd}}$ and $\mu_{^{150}\text{Nd}}$, as measured in the NaBrO₃ processed standards. No large fractionation is predicted for $\mu_{^{142}\text{Nd}}$, in agreement with our drift-corrected values. Saji et al. (2016) reported Nd isotopic fractionations by the nuclear field shift effect following the chromatographic separation of Nd on long and thin columns (80 cm length x 0.24 cm inner diameter) filled with fine Ln-spec resin (25-50 μm). They noted that the front and tail fractions of the Nd elution peak were affected by an opposite nuclear field shift effect (positive $\mu_{^{150}\text{Nd}}$ and $\mu_{^{148}\text{Nd}}$ anomalies in the front fractions and negative $\mu_{^{150}\text{Nd}}$ and $\mu_{^{148}\text{Nd}}$ in the tail fractions). Since we used the same fine Ln-spec resin in the NaBrO₃ method, but not in the MLA method, we suspect that the fractionation occurred at this stage

of the procedure. Total procedural recoveries for the JNdi-1 standards purified with the NaBrO₃ method were all above 80% but were not enough precisely constrained to evaluate whether they correlate with the amplitude of the nuclear field shift effect. The fact that our columns were much shorter (6 cm length x 0.4 cm inner diameter) than Saji's and co-workers, likely explains why the fractionation induced by the nuclear field shift is subtler in our dataset. These results call the need for a careful calibration of the fine Ln-spec column to recover the highest possible amount of Nd while ensuring a good separation of Nd from Pr. Removing the high load of Na in the Nd fraction (4th step of the NaBrO₃ method, Figure 1) before loading it on the fine Ln-spec resin (i.e. 3rd step of the NaBrO₃ method, Figure 1) may also prevent the degradation of the fine-grained resin and its calibration through time.

4.2.2. *Reference basalt BHVO-2*

Relative Nd isotopic compositions of reference basalt BHVO-2 are shown in Figure 13 and absolute ratios are provided in Appendix C. For most BHVO-2 analyses, we isolated the Nd from the matrix following the NaBrO₃ method. Only three were processed following the MLA method. Drift-corrected ratios yielded similar external precisions as those estimated from JNdi-1 standards processed through chemistry (cf. Figure 11), except for μ_{150} for which the precision is poorer for BHVO-2. The measured μ_{142} , μ_{145} , μ_{148} , and μ_{150} compositions for BHVO-2 are not resolved from the values measured for JNdi-1, which is in agreement with results from previous studies (cf. Saji et al., 2016 and Burkhardt et al., 2016 for the most recent and precise studies). For the radiogenic $^{143}\text{Nd}/^{144}\text{Nd}$ ratio, our measurements yielded $\mu_{143} = +1704.6 \pm 3.8$ (2s, n=19) ppm which is compatible, within error, with the most precise value available so far i.e. $+1698.8 \pm 2.3$ (2s) ppm from MC-ICP-MS measurements normalized to the $^{146}\text{Nd}/^{144}\text{Nd}$ ratio (n=5 aliquots measured during ~12h each at 35 V on ^{142}Nd ; Saji et al., 2016). As for the JNdi-1 Nd standards processed through the fine Ln-Spec resin, some of the drift-corrected dynamic ratios consistently deviate from zero within two standard deviations. This is in particular the case of μ_{142} and μ_{145} showing consistent excesses of about +4 and +2 ppm respectively, and μ_{150} showing a deficit of about -7 ppm (cf. Figure 13). To understand the cause of the variability, we investigated the co-variations of Nd isotope ratios in binary plots and modeled the effects of domain mixing on filaments, fractionation during chromatographic separation (i.e. nuclear field shift effect) and correlated errors (Figure 14). For domain mixing, we modeled several scenarios involving 2 or 3 domains containing variable amounts of Nd that fractionate at different rates and from different initial values. The amplitude of the resulting fractionation was of course highly

variable as a function of the scenario employed, but always followed the same slope in a given binary plot. This means that the direction of the fractionation caused by domain mixing on filaments can be predicted in Figure 14. The expected trend produced by domain mixing is shown by black arrows in each diagram. The theoretical effects of nuclear field shift were calculated following the above equation and are shown by orange arrows in Figure 14. Finally, we performed Monte-Carlo simulations to propagate counting errors on dynamic Nd isotope ratios to see whether correlated errors could explain some of the variation observed in binary plots. We calculated the Poisson errors (cf. Figure 3, Eq. 12) for each isotope beam assuming that the measurements were performed at a ^{142}Nd beam of 3V for 540 cycles, which constitutes the worst case scenario where the final 2 s.e. of the run equals 5 ppm according to Figure 3b. Then, we propagated these errors on dynamic ratios following the equations of section 2. This resulted in the ellipsoids shown in blue in the four diagrams of Figure 14. The three effects were modeled from a terrestrial composition (i.e. $\mu_i = 0$) but the direction of the variations and the ellipsoid of correlated errors can be translated in the diagrams to any given composition. This is what we did for BHVO-2 in Figures 14b and 14c since its μ_{143} composition is known to be around +1700 relative to the JNdi-1 standard (cf. Supplementary File C).

Several important conclusions can be drawn from the binary plots presented in Figure 14. First, the nuclear field shift effect is very likely responsible for the μ_{143} and μ_{145} excesses together with μ_{150} and μ_{148} deficits of some BHVO-2 processed through the fine Ln-spec resin (Figures 14b and 14d). Not all the BHVO-2 analyses are affected by the effect but the extreme compositions of four or five of them can clearly be explained by fractionation occurring during the chromatographic separation of Nd (cf. Section 4.2.1.). Secondly, both the JNdi-1 and BHVO-2 datasets show subtle positive correlations between μ_{142} and μ_{143} on the one hand, and μ_{150} and μ_{148} on the other (Figures 14a and 14d). Given the similarity of the variations produced by domain mixing effects and correlated errors, it is difficult to identify which one of the two effects is responsible for the observed positive trends. In the μ_{143} vs. μ_{145} and μ_{150} and μ_{142} isotopic spaces (Fig. 14b,c), the lack of strong correlation following the domain mixing trends argues against a large contribution of domain mixing effects. Like Andreasen and Sharma (2009), we think that the positive correlations observed between μ_{143} and μ_{142} , and between μ_{150} and μ_{148} , simply result from the propagation of counting errors. In any case, the inaccuracy caused by domain mixing on filaments is no larger than the imprecision caused by counting statistics in our dataset. We thus conclude that the most straightforward way to reduce the data variability and improve the overall precision of the

measurements is to decrease the counting errors either by measuring at higher intensities or by increasing integration times.

Since the nuclear field shift effect cannot fractionate $^{142}\text{Nd}/^{144}\text{Nd}$ ratios to a significant level and the measurements are likely not significantly affected by domain mixing effects, we cannot exclude the possibility that the subtle μ_{142} excess of about +4 that was measured for BHVO-2 is real (cf. Figure 13 and Appendix C). The dispersion of the data is too large to resolve the anomaly outside two standard deviations but the mean of the measured BHVO-2 population is statistically different from that of JNdi-1 population (p-value of $\sim 6.10^{-10}$). This would be in line with the small $^{182}\text{W}/^{184}\text{W}$ deficits measured recently in basalts from Hawaii, including BHVO-2, and indicating a mantle source formed very early in Solar System history (Mundl et al., 2017). We thus encourage future studies to report high-precision BHVO-2 measurements to see whether the +4 ppm ^{142}Nd excess that we measured here can be reproduced and eventually resolved from the bulk terrestrial composition.

5. Summary and recommendations to obtain the best accuracy and precision

In conclusion, we summarize the different points addressed above in the form of recommendations to obtain the best possible accuracy and precision for Nd isotope measurements by TIMS for amounts of Nd > 750 ng. For the chromatographic separation of Nd, we recommend that fine Ln-spec resin (25-50 μm) be used with caution since this study demonstrates that nuclear field shift effects can be induced on regular-sized quartz columns. For the measurement of a quantity of about 750 ng of Nd by TIMS, we showed that the 4-step method allows the acquisition of all ratios dynamically with an acquisition time similar to that of the common 2-step method. The method returns the best long-term precision and accuracy for all Nd isotope ratios, and additionally offers the possibility to monitor the degradation of the faraday collectors through time. Static/multistatic collection, with or without the rotation of the amplifiers, can provide good precision and accuracy when the faraday collectors are new and in good shape. However, static/multistatic ratios are ~ 100 times more sensitive to cup deterioration than dynamic ratios and the critical point at which the degradation of the faraday collectors starts to be problematic to guarantee the good quality of the static data is difficult to predict. To avoid such issues and minimize the component of imprecision and inaccuracy arising from cup deteriorations, we thus recommend that, whenever possible, isotope ratios be preferentially acquired with dynamic multicollection. During acquisition, the $^{146}\text{Nd}/^{144}\text{Nd}$ ratio should be constantly monitored to ensure that the fractionation remains normal, smooth and slow; the ideal case being that $^{146}\text{Nd}/^{144}\text{Nd}$ ratios increase at a constant

rate from 0.719-0.720 and stay below 0.724 through the ~8-hour run. After acquisition, four criteria should be checked to determine if a run was affected by domain mixing effects on filaments, was inaccurately corrected for isobaric interferences, had an unstable mean, or had inadequate counting statistics to achieve requisite precisions. Runs that do not satisfy one or more of the four criteria should be treated with caution. To make sure that the precision estimated from repeated measurements of standards is applicable to samples, dynamic Nd isotope ratios should be systematically corrected for drift in between acquisition lines.

Acknowledgements

We thank Chantal Bosq (LMV, Clermont-Ferrand, France) for ensuring optimal working conditions in the clean laboratory, Jean-Luc Piro (LMV, Clermont-Ferrand, France) for assistance with quadrupole ICP-MS, Régis Doucelance (LMV, Clermont-Ferrand, France), Catherine Chauvel (IPGP, Paris, France), Steven B. Shirey (Carnegie Institution for Science, Washington D.C., United States), Anne Trinquier (ETH Zurich, Switzerland) and David Cook (ETH Zurich, Switzerland) for fruitful discussions on the results of this study. Klaus Mezger is acknowledged for his editorial work. Mukul Sharma and an anonymous reviewer are thanked for their constructive comments that helped improve the quality of the manuscript. This study was funded by the Carnegie Institution for Science, the French Government Laboratory of Excellence initiative n°ANR-10-LABX-0006, the Région Auvergne, the European Regional Development Fund and the Swiss National Science Foundation (SNSF). This project has received funding from the SNSF Ambizione fellowship program under grant N° PZ00P2_161218 and from the European Union's Horizon 2020 research and innovation program under Grant Agreement N° 682778. This is Laboratory of Excellence ClerVolc contribution N° 275.

Table captions

Table 1: Collector configurations used for the 4-line method

Table 2: Example of the ratios calculated for each run using the Matlab® routine

Table 3: Suggested reference values for the absolute Nd isotopic composition of the JNdi-1 Nd reference standard measured by TIMS. These values correspond to the mean of the Nd isotope ratios (n = 54) measured over a period of ~1.5 years using the 4-step method on three

different instruments (Triton™ Carnegie, Triton™ LMV, and Triton Plus™ LMV). Our preferred values (drift-corrected dynamic ratios) are indicated in bold.

Table 4: Mean dynamic ratios of the JNdi-1 Nd reference standards gathered in five groups as a function of the instrument and the age of the faraday cups. We used the values reported in this table to calculate μ values shown in Figures 9 to 14.

Figure captions

Figure 1: Organization charts showing the different steps of the two chemical procedures followed to separate Nd from the sample matrix.

Figure 2: Panels a) and b) Deviations of $^{142}\text{Nd}/^{144}\text{Nd}$ ratios from the exponential law against $^{146}\text{Nd}/^{144}\text{Nd}$ ratios for two individual runs of the JNdi-1 Nd reference standard. $^{142}\text{Nd}/^{144}\text{Nd}$ and $^{146}\text{Nd}/^{144}\text{Nd}$ ratios are corrected for gain, baseline and isobaric interferences. The asterisks shown in panels a and b correspond to 20-point moving averages that allows for a better identification of the trend followed by the two ratios during the run. In gray are shown the ratios used to calculate the 1st dynamic $^{142}\text{Nd}/^{144}\text{Nd}$ ratio (i.e. $^{142}\text{Nd}/^{144}\text{Nd}_{\text{Meas } 1}$ vs. $^{146}\text{Nd}/^{144}\text{Nd}_{\text{Meas } 3}$). In blue are shown the ratios normally used to calculate the 2nd dynamic $^{142}\text{Nd}/^{144}\text{Nd}$ ratio (i.e. $^{142}\text{Nd}/^{144}\text{Nd}_{\text{Meas } 2}$ vs. $^{146}\text{Nd}/^{144}\text{Nd}_{\text{Meas } 4}$). The theoretical evolution of the ratios following different fractionation laws were calculated assuming that the true $^{142}\text{Nd}/^{144}\text{Nd}$ value of the JNdi-1 standard was equal to 1.141832 and $^{146}\text{Nd}/^{144}\text{Nd} = 0.7219$ (see Carlson, 2014 for the equations of the common fractionation laws). **Panels c) and d)** Evolution of $^{146}\text{Nd}/^{144}\text{Nd}$ ratios (acquisition line 3) during the JNdi-1 runs shown in panels a) and b), respectively.

Figure 3: Relationship between mean run intensities, standard deviations and minimum number of ratios to establish a mean $^{142}\text{Nd}/^{144}\text{Nd}$ ratio at ± 5 ppm and ± 3 ppm with 95% confidence.

a) Mean ^{142}Nd intensities of JNdi-1 runs vs. standard deviations returned by the 4-step method for dynamic $^{142}\text{Nd}/^{144}\text{Nd}$ ratios. Data points correspond to individual runs of JNdi-1 Nd reference standards (n =54, data available in Appendix A). Standard deviations shown on

the x-axis were calculated on all dynamic $^{142}\text{Nd}/^{144}\text{Nd}$ ratios (i.e. $\left(\frac{^{142}\text{Nd}}{^{144}\text{Nd}}\right)_{\text{Dyn 1}}$ and $\left(\frac{^{142}\text{Nd}}{^{144}\text{Nd}}\right)_{\text{Dyn 2}}$ pooled together). Details on how the Monte-Carlo simulations were performed to predict Poisson noise can be found in the main text. **b)** Theoretical relationship between mean ^{142}Nd run intensities and minimum number of ratios to measure to establish a mean dynamic $^{142}\text{Nd}/^{144}\text{Nd}$ ratio (i.e. $\left(\frac{^{142}\text{Nd}}{^{144}\text{Nd}}\right)_{\text{Dyn 1}}$ and $\left(\frac{^{142}\text{Nd}}{^{144}\text{Nd}}\right)_{\text{Dyn 2}}$ pooled together) at ± 5 ppm, and ± 3 ppm with 95% confidence. See text for more details.

Figure 4: Stabilization of the mean of dynamic $^{142}\text{Nd}/^{144}\text{Nd}$ ratios through a run (panels a-b) compared to the evolution of the mass fractionation as recorded by the measured $^{146}\text{Nd}/^{144}\text{Nd}$ ratios through the same runs (panels c-d).

Panels a-c and b-d show ratios acquired during two individual runs of the JNdi-1 Nd standard. **a) -b)** Deviations shown on the y-axis are calculated relative to the mean of all dynamic $^{142}\text{Nd}/^{144}\text{Nd}$ ratios ($\left(\frac{^{142}\text{Nd}}{^{144}\text{Nd}}\right)_{\text{Dyn 1}}$ and $\left(\frac{^{142}\text{Nd}}{^{144}\text{Nd}}\right)_{\text{Dyn 2}}$ pooled together) returned by the 4-line method at the end of the run. The green horizontal bands show the final standard errors of the dynamic $^{142}\text{Nd}/^{144}\text{Nd}$ ratios ($\left(\frac{^{142}\text{Nd}}{^{144}\text{Nd}}\right)_{\text{Dyn 1}}$ and $\left(\frac{^{142}\text{Nd}}{^{144}\text{Nd}}\right)_{\text{Dyn 2}}$ pooled together) at the end of the run. For the run shown in panel a), the mean of all dynamic $^{142}\text{Nd}/^{144}\text{Nd}$ ratios quickly reaches a plateau and converges to one value at the end of the run. For the run shown in panel b), the mean of all dynamic $^{142}\text{Nd}/^{144}\text{Nd}$ ratios does not converge to a stable value but continuously increases after ~ 300 cycles until the end of the run, perhaps due to domain mixing on filament. **c) -d)** Evolution of $^{146}\text{Nd}/^{144}\text{Nd}$ ratios (acquisition line 3) through the runs.

Figure 5: Propagated errors generated by imprecise correction of isobaric interferences on dynamic Nd isotope ratios.

Monte-Carlo simulations were performed assuming that the fractionation factor f of Ce and Sm isotope ratios varied between -1 and +1 during measurement. Imprecisions become $\geq \pm 5$ ppm on the dynamic $^{142}\text{Nd}/^{144}\text{Nd}$ ratio when the $^{140}\text{Ce}/^{146}\text{Nd}$ ratio is higher than 0.0016 and $\geq \pm 5$ ppm on the dynamic $^{150}\text{Nd}/^{144}\text{Nd}$ ratio when the $^{147}\text{Sm}/^{146}\text{Nd}$ ratio is higher than 0.00012.

Figure 6: Principle of the drift-correction for dynamic isotope ratios

For each acquisition line i , the evolution of $^{146}\text{Nd}/^{144}\text{Nd}$ ratios through time is approximated to be linear over 11 consecutive cycles so that $\left(\frac{^{146}\text{Nd}}{^{144}\text{Nd}}\right)_{N,i} = (F_R)_{N,i} \times t + C_{N,i}$, where $(F_R)_{N,i}$ is the fractionation rate that can be expressed in ppm.s^{-1} (see Appendix A-B-C), t is the time after the start of the run (in seconds) and $C_{N,i}$ is a constant. $(F_R)_{N,i}$ and $C_{N,i}$ are determined offline when the run is completed for each acquisition line i of each cycle N using a least-square regression over 11 points (5 cycles before N , the cycle N in question, and 5 cycles after N). With this equation the value of the $^{146}\text{Nd}/^{144}\text{Nd}$ ratio from any acquisition line i can be recalculated at the desired time t for each cycle N .

Figure 7: Compilation of dynamic and static Nd isotope ratios measured in JNdi-1 Nd standards ($n = 54$) over a period of ~ 1.5 years on three different instruments.

Data points correspond to individual runs of the JNdi-1 Nd reference standard ($n = 54$, data available in Appendix A). Horizontal error bars represent 2 standard errors. The horizontal solid lines separate the analyses performed on different instruments while the horizontal dashed line indicates a change of all faraday collectors including the axial cup.

Figure 8: Effect of faraday collector deterioration on static isotope ratios.

Data points correspond to individual runs of JNdi-1 Nd reference standard ($n = 54$, data available in Appendix A). Horizontal and vertical error bars represent 2 standard errors. Static $^{142}\text{Nd}/^{144}\text{Nd}$ and $^{148}\text{Nd}/^{144}\text{Nd}$ ratios were corrected for mass fractionation following the exponential law using ratios from acquisition lines 1 and 3, respectively. See text in section 4.1.3.1. for more details. The grey dashed line (mass fractionation line) was calculated using the exponential law and a normalization to $^{142}\text{Nd}/^{144}\text{Nd} = 1.181432$ and $^{148}\text{Nd}/^{144}\text{Nd} = 0.241581$ (dynamic drift-corrected ratios, Table 3).

Figure 9: Relationship between mean fractionation rates and dynamic $^{142}\text{Nd}/^{144}\text{Nd}$ ratios.

Data points correspond to individual runs of the JNdi-1 Nd reference standard (data available in Appendix A and B). Horizontal error bars represent 2 standard errors. The mean fractionation rate of a run is calculated by averaging the fractionation rate $(F_R)_{N,3}$ calculated at each cycle from $^{146}\text{Nd}/^{144}\text{Nd}_{\text{Meas } 3}$ (i.e. by averaging the slopes of the linear trends formed by 11 consecutive measurements of $^{146}\text{Nd}/^{144}\text{Nd}_{\text{Meas } 3}$; cf. caption of Figure 6). Dynamic μ_{142} values correspond to the mean of the two dynamic $^{142}\text{Nd}/^{144}\text{Nd}$ ratios returned by the 4-step method and were calculated relative to mean JNdi-1 values reported in Table 4. Pink

diamonds with blue and yellow dots inside correspond to JNdi-1 Nd standard processed through column chemistry following the MLA and NaBrO₃ methods, respectively (data available in Appendix B)

Figure 10: Effect of the drift correction on the precision of dynamic Nd isotope ratios.

Data points correspond to individual runs of the JNdi-1 Nd standard (n = 54, data available in Appendix A). Horizontal error bars represent 2 standard errors. Vertical gray bands represent 2 standard deviations (2s) calculated from relative values.

Figure 11: Relative Nd isotopic compositions of JNdi-1 Nd standards processed through column chemistry following the MLA and NaBrO₃ methods.

Data points correspond to individual runs of JNdi-1 Nd standards measured on the LMV Triton Plus[™] in November 2016. Horizontal error bars represent 2 standard errors. Absolute Nd isotopic compositions are provided in Appendix B. Vertical colored bands represent 2 standard deviations (2s) calculated from relative values for each group of data.

Figure 12: Nuclear field shift effect on Nd isotopes

a) Same data as in Figure 11. **b)** Theoretical effects of the nuclear field shift on Nd isotope ratios for different values of the scaling factor α . See equation in section 4.2.1.

Figure 13: Relative Nd isotopic compositions of reference standard BHVO-2 processed through different chemistries (MLA and NaBrO₃ methods).

Data points correspond to individual runs of reference basalt BHVO-2 (n = 19, data available in Appendix C). Horizontal error bars represent 2 standard errors. Vertical gray bands represent 2 standard deviations (2s) calculated from relative values.

Figure 14: Binary plots used to investigate the main sources of residual variability for drift-corrected dynamic isotope ratios.

Data points correspond to individual runs of reference basalts BHVO-2 or JNdi-1 Nd standards (data in Appendix B and C). Colors and symbols as in Figures 11 and 13. Error bars represent 2 standard errors. Domain mixing effects and correlated errors from counting statistics were modeled using Monte-Carlo simulations (see text in section 4.2.2. for more details). Nuclear field shift effects were modeled using the equation reported in section 4.2.1.

References

- Andreasen, R., Sharma, M., 2009. Fractionation and mixing in a thermal ionization mass spectrometer source: Implications and limitations for high-precision Nd isotope analyses. *International Journal of Mass Spectrometry* 285, 49–57. doi:10.1016/j.ijms.2009.04.004
- Andreasen, R., Sharma, M., 2006. Solar nebula heterogeneity in p-process samarium and neodymium isotopes. *Science* 314, 806–809. doi:10.1126/science.1132941
- Bennett, V.C., Brandon, A.D., NUTMAN, A.P., 2007. Coupled ^{142}Nd - ^{143}Nd isotopic evidence for Hadean mantle dynamics. *Science* 318, 1907–1910. doi:10.1126/science.1109087
- Bouvier, A., Boyet, M., 2016. Primitive Solar System materials and Earth share a common initial ^{142}Nd abundance. *Nature* 537, 399–402. doi:10.1038/nature19351
- Boyet, M., Carlson, R.W., 2005. ^{142}Nd Evidence for Early (>4.53 Ga) Global Differentiation of the Silicate Earth. *Science* 309, 576–581. doi:10.1126/science.1113634
- Brandon, A.D., Lapen, T.J., Debaille, V., Beard, B.L., Rankenburg, K., Neal, C., 2009. Re-evaluating $^{142}\text{Nd}/^{144}\text{Nd}$ in lunar mare basalts with implications for the early evolution and bulk Sm/Nd of the Moon. *Geochimica et Cosmochimica Acta* 73, 6421–6445. doi:10.1016/j.gca.2009.07.015
- Burkhardt, C., Borg, L.E., Brennecka, G.A., 2016. A nucleosynthetic origin for the Earth's anomalous ^{142}Nd composition. *Nature* 537, 394–398. doi:10.1038/nature18956
- Carlson, R.W., 2014. 15.18 Thermal Ionization Mass Spectrometry, in: Holland, H., Turekian, K. (Eds.), *Treatise on Geochemistry (Second Edition)*. Elsevier Ltd., pp. 337–354. doi:10.1016/B978-0-08-095975-7.01427-3
- Carlson, R.W., Boyet, M., Horan, M., 2007. Chondrite Barium, Neodymium, and Samarium Isotopic Heterogeneity and Early Earth Differentiation. *Science* 316, 1175–1178. doi:10.1126/science.1140189
- Chang, T.L., Qian, Q.Y., Zhao, M.T., Wang, J., Lang, Q.Y., 1995. The Absolute Isotopic Composition of Cerium. *International Journal of Mass Spectrometry and Ion Processes* 142, 125–131. doi:10.1016/0168-1176(95)90677-A
- Chang, T.L., Zhao, M.T., Li, W.J., Wang, J., Qian, Q.Y., 2002. Absolute isotopic composition and atomic weight of samarium. *International Journal of Mass Spectrometry* 218, 167–172. doi:10.1016/S1387-3806(02)00665-6
- Cook, D.L., Schönbächler, M., 2016. High-precision measurement of W isotopes in Fe–Ni alloy and the effects from the nuclear field shift. *J. Anal. At. Spectrom.* 31, 1400–1405. doi:10.1039/C6JA00015K
- Fujii, T., Moynier, F., Albarede, F., 2009. The nuclear field shift effect in chemical exchange reactions. *Chemical Geology*. doi:10.1016/j.chemgeo.2009.06.015
- Fujii, T., Moynier, F., Albarede, F., 2006. Nuclear field vs. nucleosynthetic effects as cause of isotopic anomalies in the early Solar System. *Earth and Planetary Science Letters* 247, 1–9. doi:10.1016/j.epsl.2006.04.034
- Fujii, T., Yamamoto, T., Inagawaa, J., Gunji, K., 2000. Nuclear size and shape effects in chemical isotope enrichment of neodymium using a crown ether. *Solvent Extraction and Ion Exchange*. doi:10.1080/07366290008934726
- Fukai, R., Yokoyama, T., Kagami, S., 2017. Evaluation of the long-term fluctuation in isotope

- ratios measured by TIMS with the static, dynamic, and multistatic methods: A case study for Nd isotope measurements. *International Journal of Mass Spectrometry* 414, 1–7. doi:10.1016/j.ijms.2016.12.016
- Garçon, M., Sauzéat, L., Carlson, R.W., Shirey, S.B., Simon, M., Balter, V., Boyet, M., 2017. Nitrile, Latex, Neoprene and Vinyl Gloves: A Primary Source of Contamination for Trace Element and Zn Isotopic Analyses in Geological and Biological Samples. *Geostandards and Geoanalytical Research* 47, 3, 367–380. doi:10.1111/ggr.12161
- Hart, S.R., Zindler, A., 1989. Isotope Fractionation Laws - a Test Using Calcium. *International Journal of Mass Spectrometry and Ion Processes* 89, 287–301. doi:10.1016/0168-1176(89)83065-4
- Heilig, K., Fricke, G., 2004. Volume 20 Nuclear Charge Radii, in: Schopper, H. (Ed.), *Landolt-Börnstein - Group I Elementary Particles, Nuclei and Atoms*, 60-Nd Neodymium.
- Li, C.-F., Wang, X.-C., Li, Y.-L., Chu, Z.-Y., Guo, J.-H., Li, X.-H., 2015. Ce–Nd separation by solid-phase micro-extraction and its application to high-precision $^{142}\text{Nd}/^{144}\text{Nd}$ measurements using TIMS in geological materials. *J. Anal. At. Spectrom.* 30, 895–902. doi:10.1039/C4JA00328D
- Makishima, A., Nakamura, E., 1991. Calibration of Faraday cup efficiency in a multicollector mass spectrometer. *Chemical Geology* 94, 105–110. doi:10.1016/S0009-2541(10)80022-1
- Morino, P., Caro, G., Reisberg, L., Schumacher, A., 2017. Chemical stratification in the post-magma ocean Earth inferred from coupled ^{146}Sm – ^{142}Nd systematics in ultramafic rocks of the Saglek block (3.25–3.9 Ga; northern Labrador, Canada). *Earth and Planetary Science Letters* 463, 136–150. doi:10.1016/j.epsl.2017.01.044
- Mundl, A., Touboul, M., Jackson, M.G., Day, J.M.D., Kurz, M.D., Lekic, V., Helz, R.T., Walker, R.J., 2017. Tungsten-182 heterogeneity in modern ocean island basalts. *Science* 356, 66–. doi:10.1126/science.aal4179
- O'Neil, J., Carlson, R.W., Francis, D., Stevenson, R.K., 2008. Neodymium-142 evidence for Hadean mafic crust. *Science* 321, 1828–1831. doi:10.1126/science.1159582
- Rizo, H., Boyet, M., Blichert-Toft, J., O'Neil, J., Rosing, M.T., Paquette, J.-L., 2012. The elusive Hadean enriched reservoir revealed by ^{142}Nd deficits in Isua Archaean rocks. *Nature* 490, 96–100. doi:10.1038/nature11565
- Roth, A.S.G., Bourdon, B., Mojzsis, S.J., Touboul, M., Sprung, P., Guitreau, M., Blichert-Toft, J., 2013. Inherited ^{142}Nd anomalies in Eoarchean protoliths. *Earth and Planetary Science Letters* 361, 50–57. doi:10.1016/j.epsl.2012.11.023
- Roth, A.S.G., Scherer, E.E., Maden, C., Mezger, K., Bourdon, B., 2014. Revisiting the ^{142}Nd deficits in the 1.48Ga Khariar alkaline rocks, India. *Chemical Geology* 386, 238–248. doi:10.1016/j.chemgeo.2014.06.022
- Russell, W.A., Papanastassiou, D.A., Tombrello, T.A., 1978. Ca Isotope Fractionation on Earth and Other Solar-System Materials. *Geochimica et Cosmochimica Acta* 42, 1075–1090. doi:10.1016/0016-7037(78)90105-9
- Saji, N.S., Wielandt, D., Paton, C., Bizzarro, M., 2016. Ultra-high-precision Nd-isotope measurements of geological materials by MC-ICPMS. *J. Anal. At. Spectrom.* 31, 1490–1504. doi:10.1039/C6JA00064A

- Sharma, M., Papanastassiou, D. A., Wasserburg, G. J., Dymek R. F., 1996. The issue of the Terrestrial record of ^{146}Sm . *Geochimica et Cosmochimica Acta* 60, 1, 2037–2047.
- Sharma, M., Chen, C., 2004. Neodymium isotope fractionation in the mass spectrometer and the issue of ^{142}Nd anomalies in early Archean rocks. *Precambrian Research* 135, 315–329. doi:10.1016/j.precamres.2004.09.003
- Tanaka, T., Togashi, S., Kamioka, H., Amakawa, H., Kagami, H., Hamamoto, T., Yuhara, M., Orihashi, Y., Yoneda, S., Shimizu, H., Kunimaru, T., Takahashi, K., Yanagi, T., Nakano, T., Fujimaki, H., Shinjo, R., Asahara, Y., Tanimizu, M., Dragusanu, C., 2000. JNdi-1: a neodymium isotopic reference in consistency with LaJolla neodymium. *Chemical Geology* 168, 279–281.
- Tazoe, H., Obata, H., Gamo, T., 2007. Determination of cerium isotope ratios in geochemical samples using oxidative extraction technique with chelating resin. *J. Anal. At. Spectrom.* 22, 616–7. doi:10.1039/b617285g
- Thirlwall, M.F., 1991. Long-term reproducibility of multicollector Sr and Nd isotope ratio analysis. *Chemical Geology* 94, 85–104. doi:10.1016/S0009-2541(10)80021-X
- Upadhyay, D., Scherer, E.E., Mezger, K., 2009. ^{142}Nd evidence for an enriched Hadean reservoir in cratonic roots. *Nature* 459, 1118–1121. doi:10.1038/nature08089
- Upadhyay, D., Scherer, E.E., Mezger, K., 2008. Fractionation and mixing of Nd isotopes during thermal ionization mass spectrometry: implications for high precision $^{142}\text{Nd}/^{144}\text{Nd}$ analyses. *J. Anal. At. Spectrom.* 23, 561–8. doi:10.1039/b715585a
- Wakaki, S., Tanaka, T., 2012. Stable isotope analysis of Nd by double spike thermal ionization mass spectrometry. *International Journal of Mass Spectrometry* 323–324, 45–54. doi:10.1016/j.ijms.2012.06.019
- Wang, M., Audi, G., Wapstra, A.H., Kondev, F.G., MacCormick, M., Xu, X., Pfeiffer, B., 2012. The Ame2012 atomic mass evaluation. *Chinese Phys. C* 36, 1603–2014. doi:10.1088/1674-1137/36/12/003
- Wielandt, D., Bizzarro, M., 2011. A TIMS-based method for the high precision measurements of the three-isotope potassium composition of small samples. *J. Anal. At. Spectrom.* 26, 366–377. doi:10.1039/c0ja00067a
- Yang, S., Liu, Y., 2016. Nuclear field shift effects on stable isotope fractionation: a review. *Acta Geochimica* 35, 227–239. doi:10.1007/s11631-016-0109-3

Figure 1

MLA Method

1st Step

Separation of the LREE from the matrix using cation resin AG50W-X8 (200-400 mesh) and HCl 2N to 6N
Duration: ~ 10 hours

2nd Step

Separation of Nd from other LREE using cation resin AG50W-X8 (100-200 mesh) and 2-MLA acid under pressure (N_2)
Duration: ~ 2 × 7 hours

3rd Step

Purification of Nd (mainly to remove residual Sm) using Ln-Spec resin (50-100 μ m) and HCl 0.175N
Duration: ~ 10 hours

NaBrO₃ Method

1st Step

Separation of the LREE from the matrix using cation resin AG50W-X8 (200-400 mesh) and HCl 2N to 6N
Duration: ~ 10 hours

2nd Step

Removal of Ce using Ln-Spec resin (100-150 μ m) and HNO_3 10N + $NaBrO_3$ 20nM
Duration: ~ 2 × 2 hours

3rd Step

Separation of Nd from other LREE using fine-grained Ln-Spec resin (25-50 μ m) and HCl 0.2N to 0.25N

4th Step

Purification of Nd (mainly to remove residual Na, Br and Ba) using cation resin AG50W-X8 (200-400 mesh) and HNO_3 2N, HCl 2.5N to 6N
Duration: ~ 4 hours

Figure 2

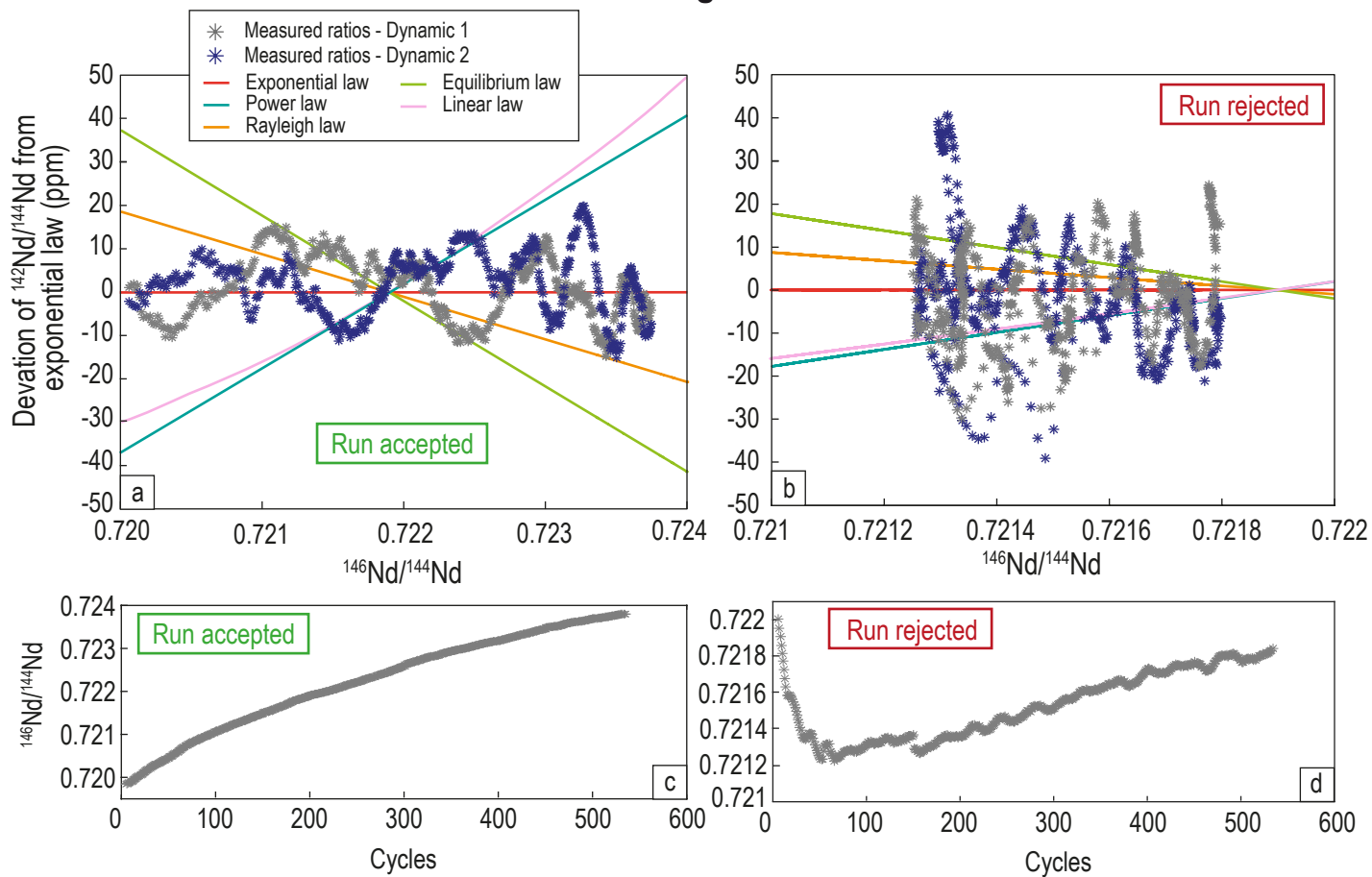


Figure 3

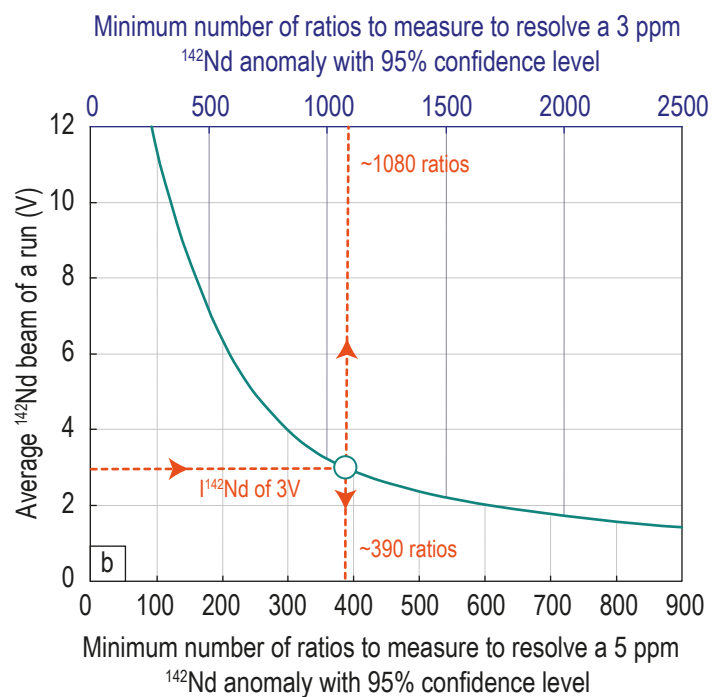
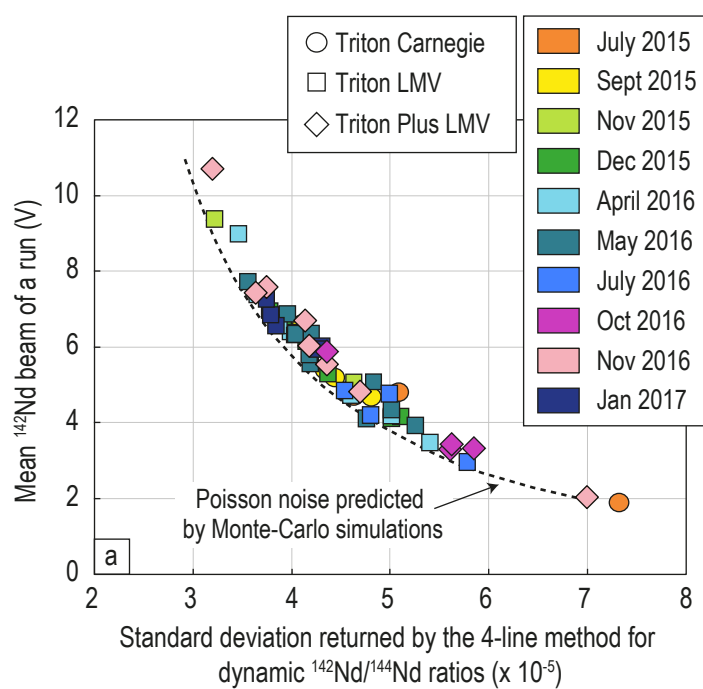


Figure 4

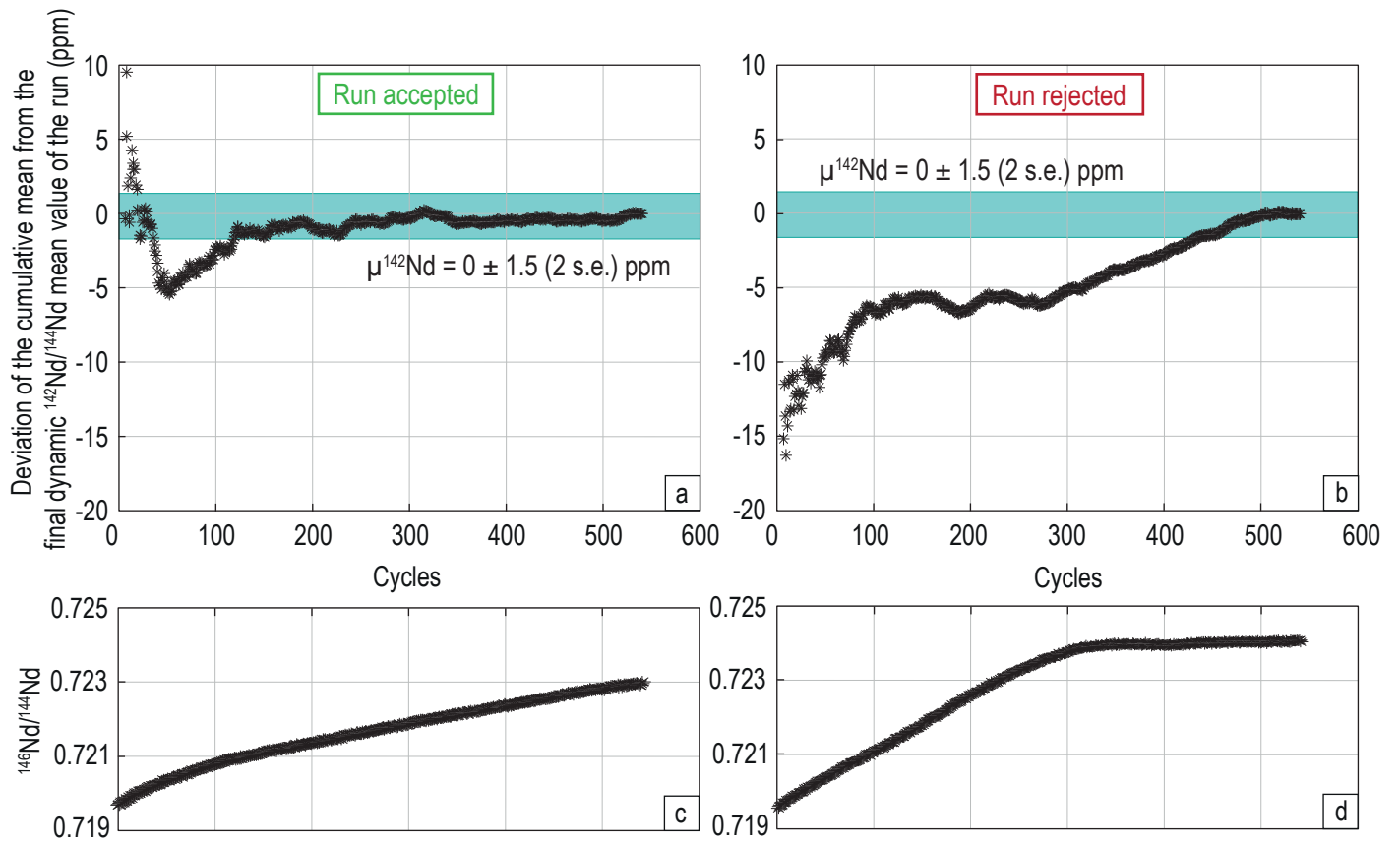


Figure 5

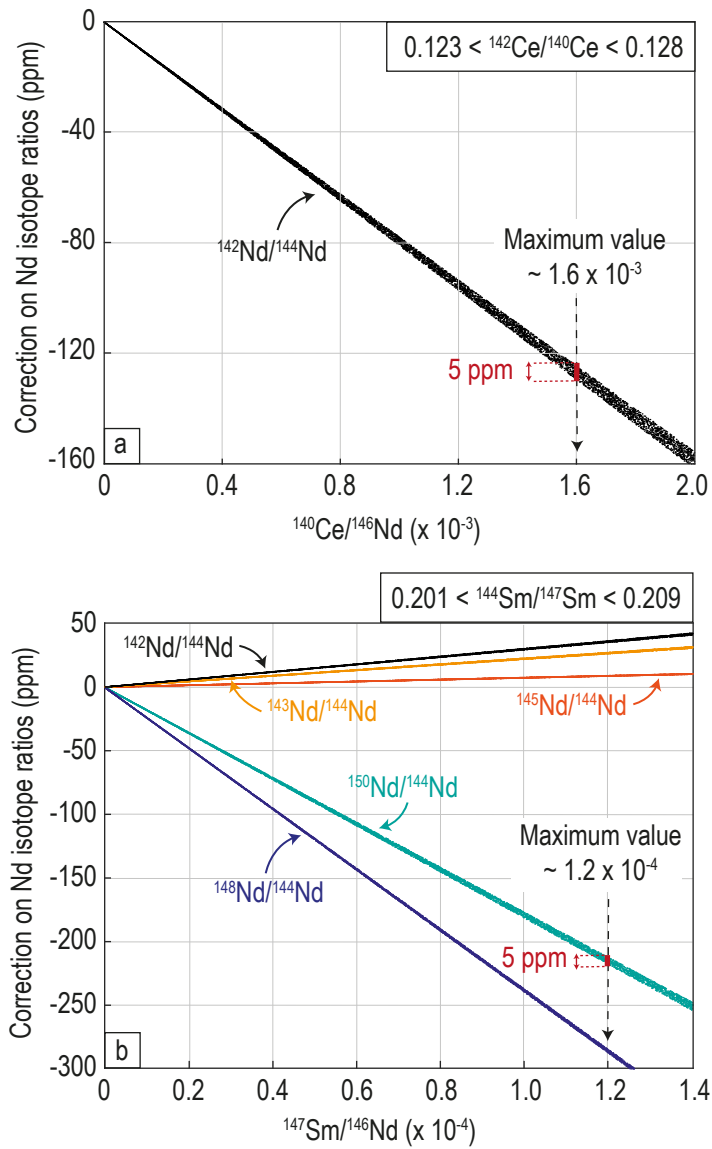


Figure 6

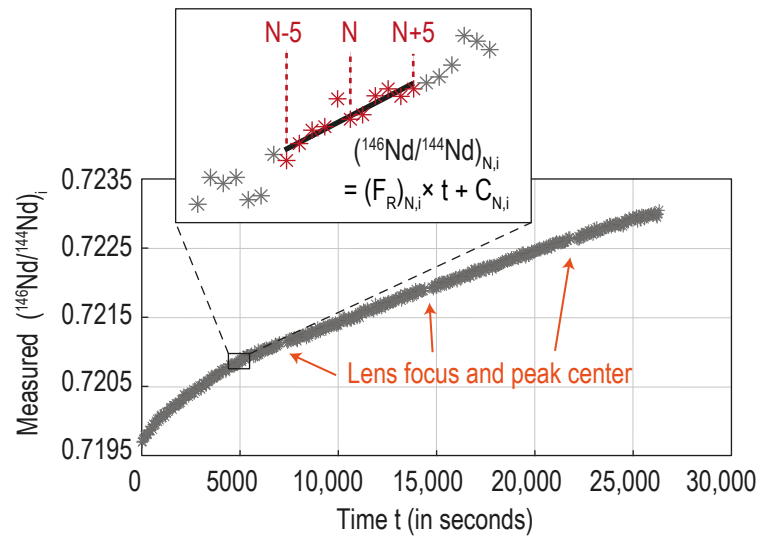


Figure 7

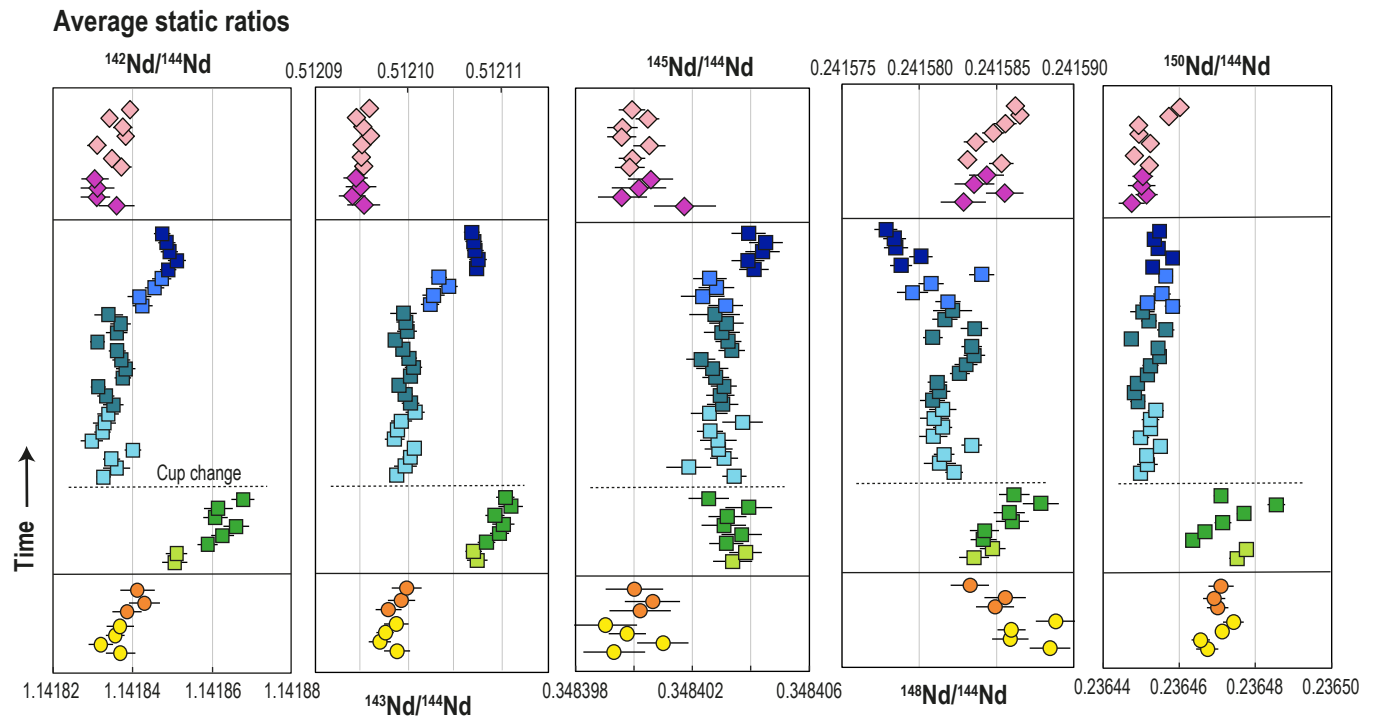
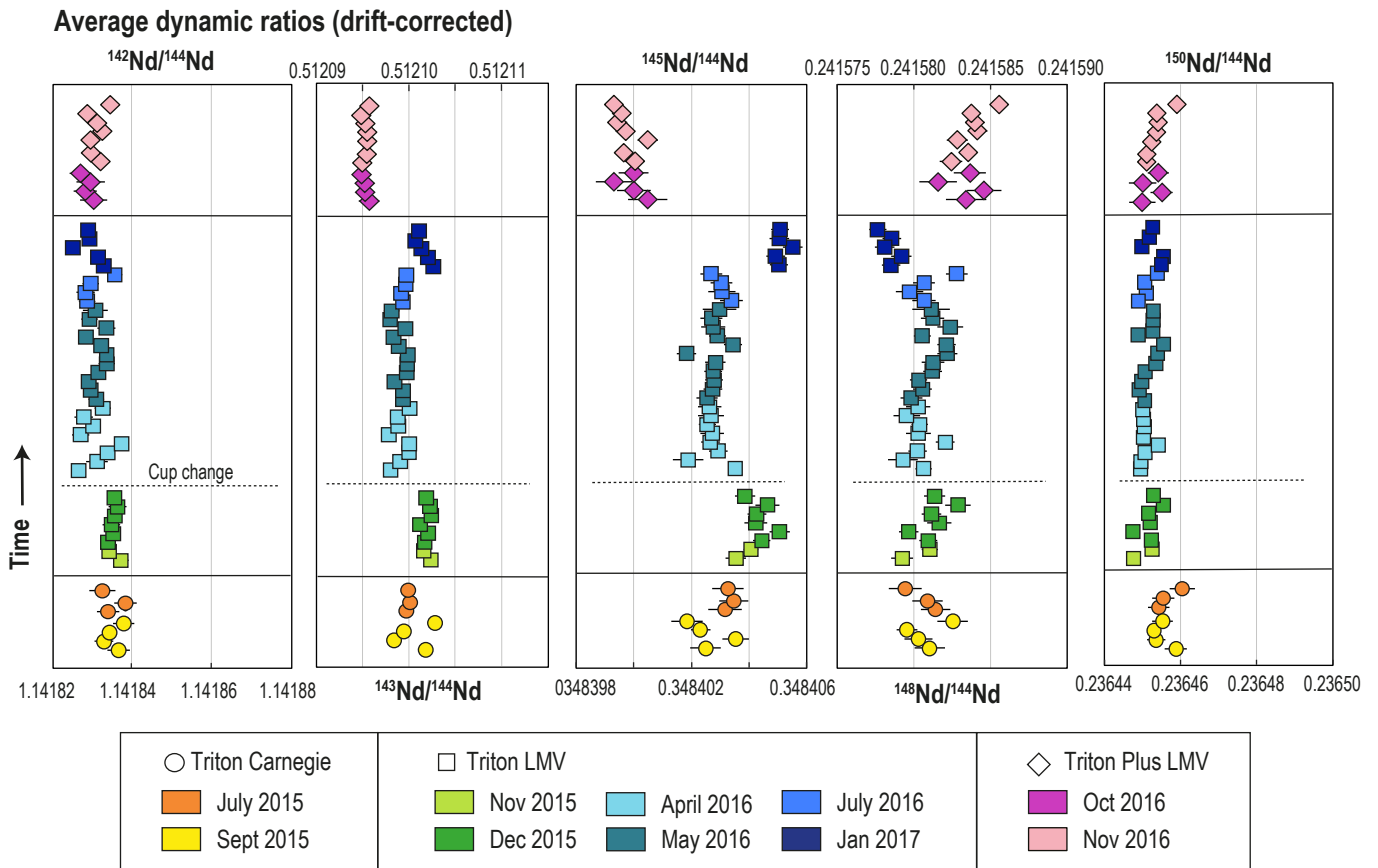


Figure 8

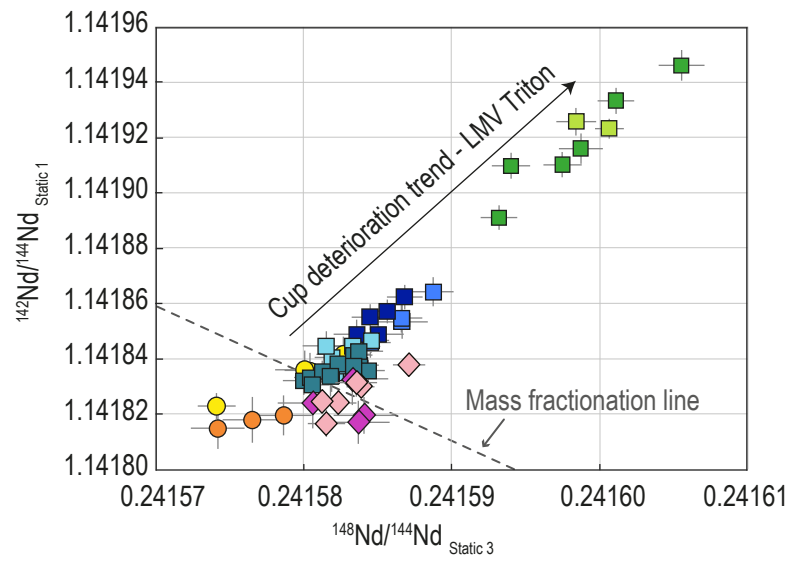


Figure 9

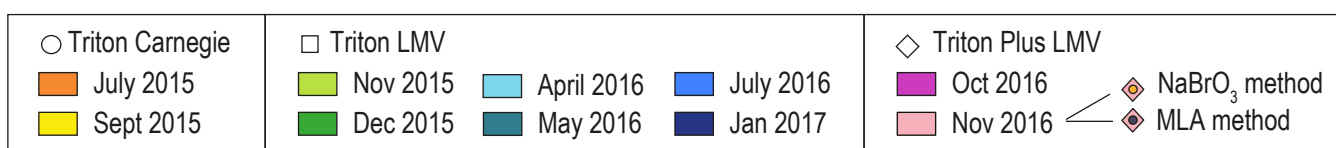
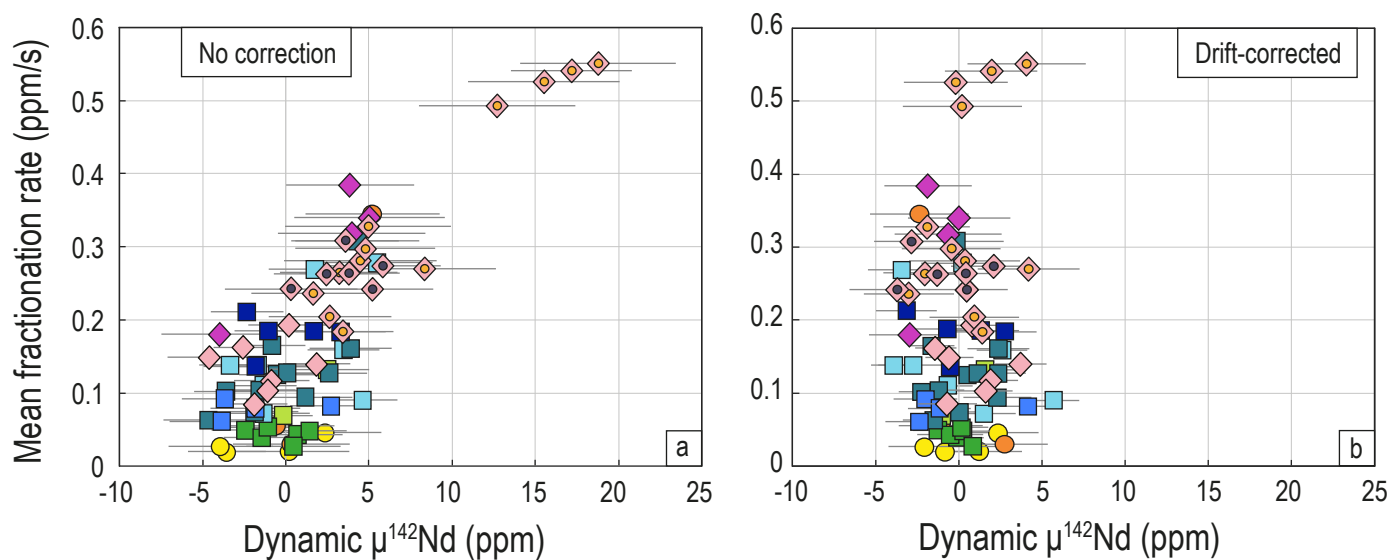
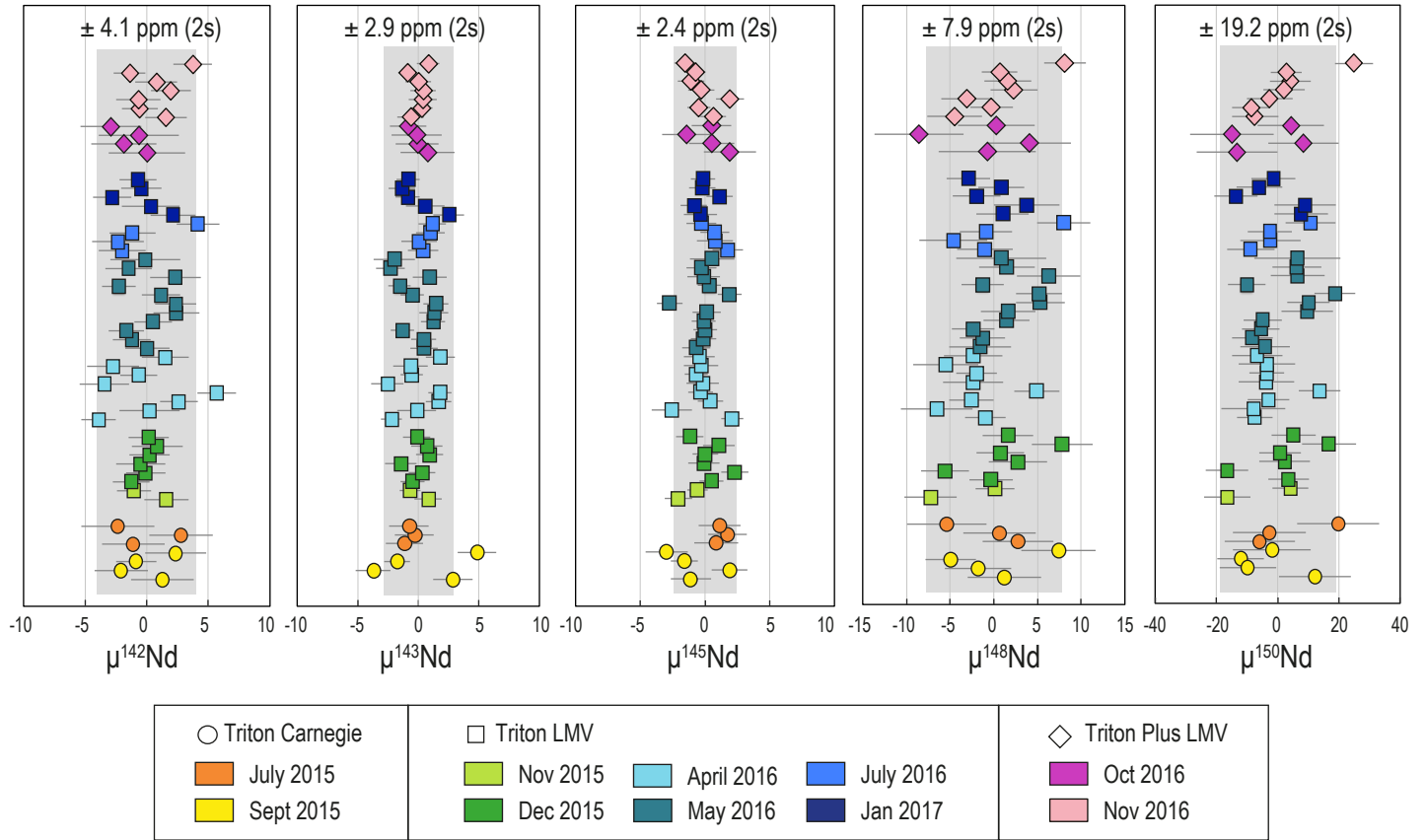


Figure 10

Average dynamic ratios (drift-corrected)



Average dynamic ratios (no correction)

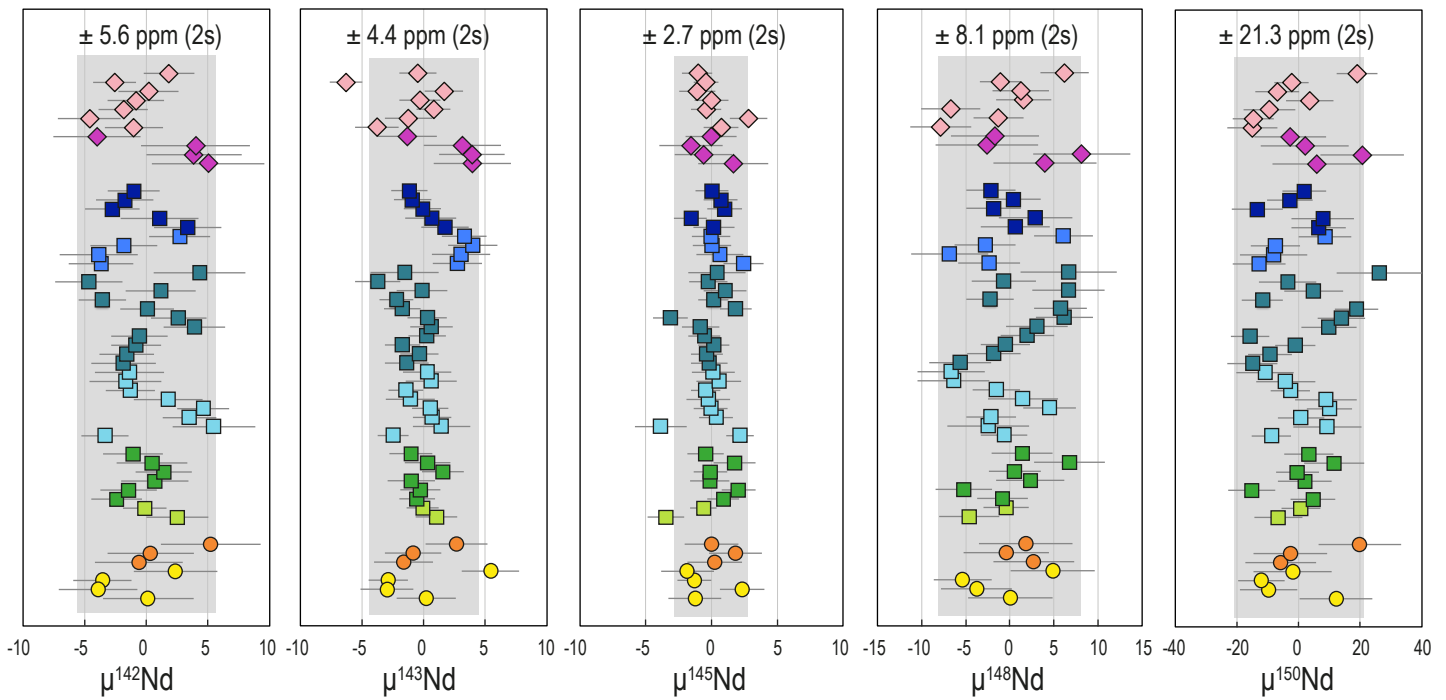
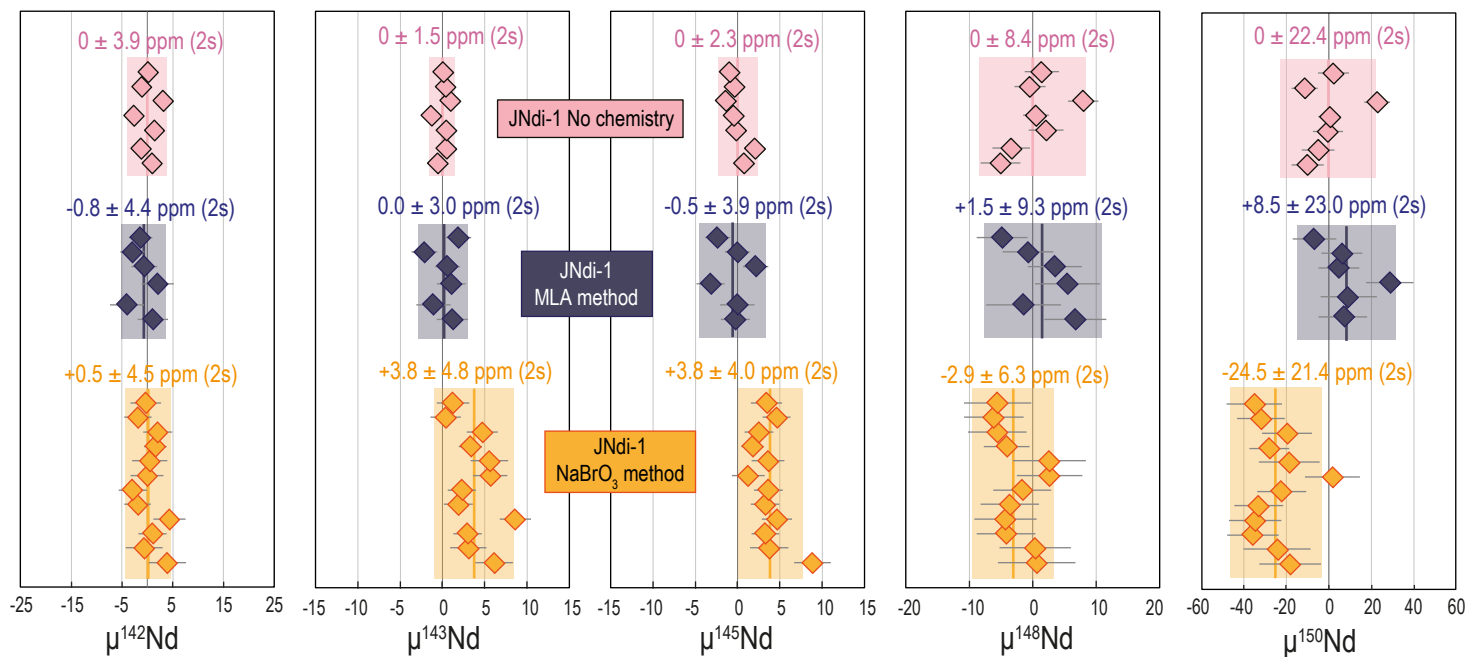


Figure 11

Average dynamic ratios (drift-corrected)



Average dynamic ratios (no correction)

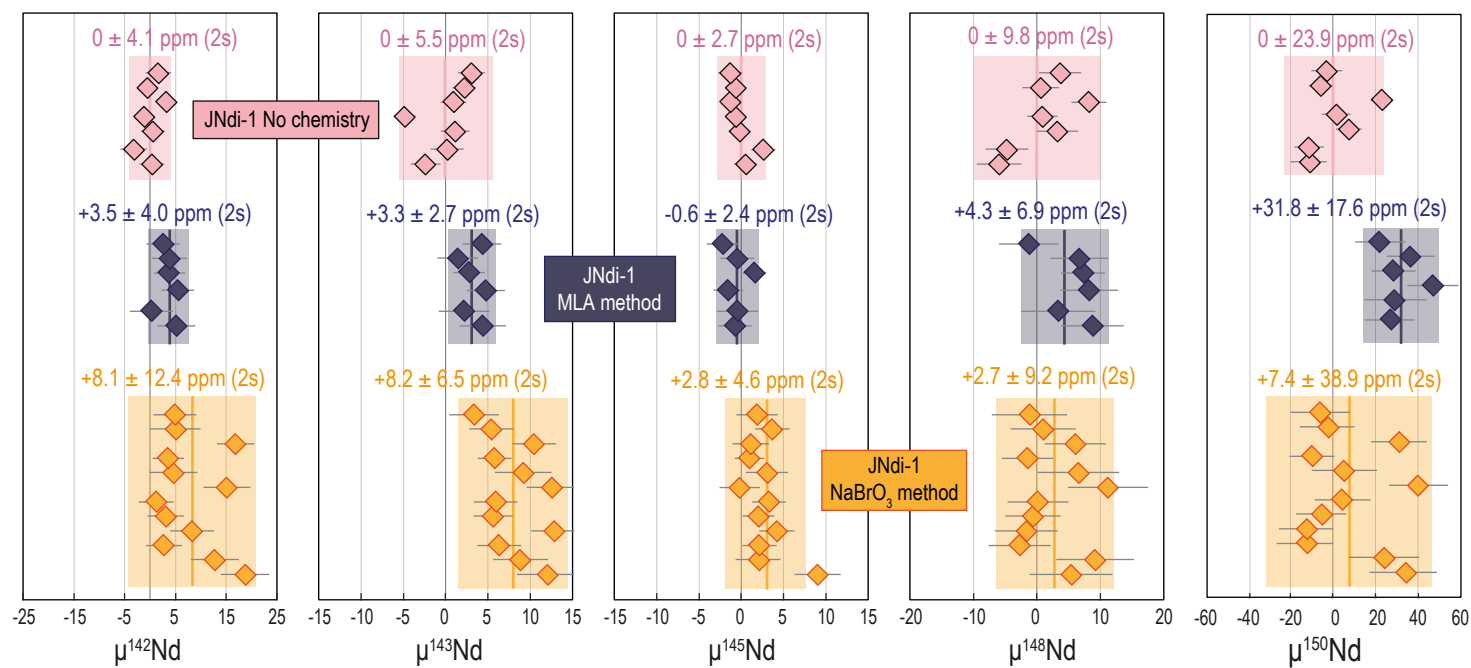


Figure 12

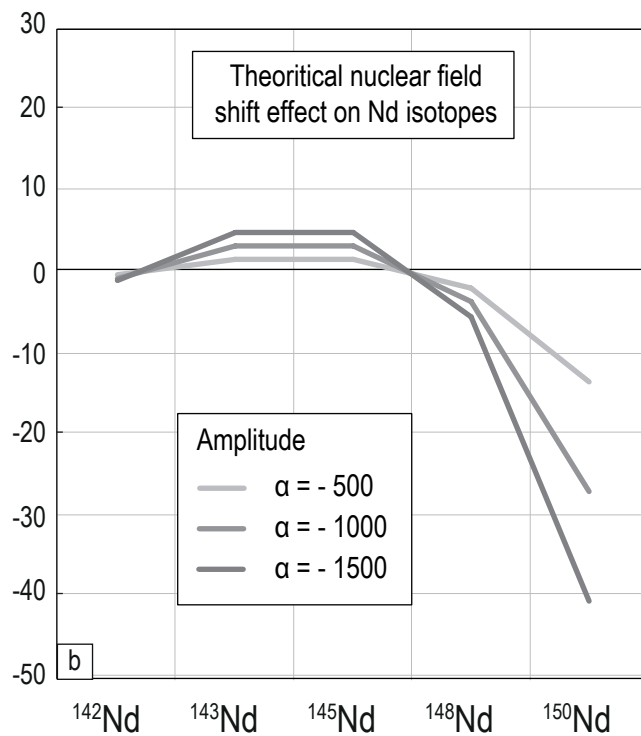
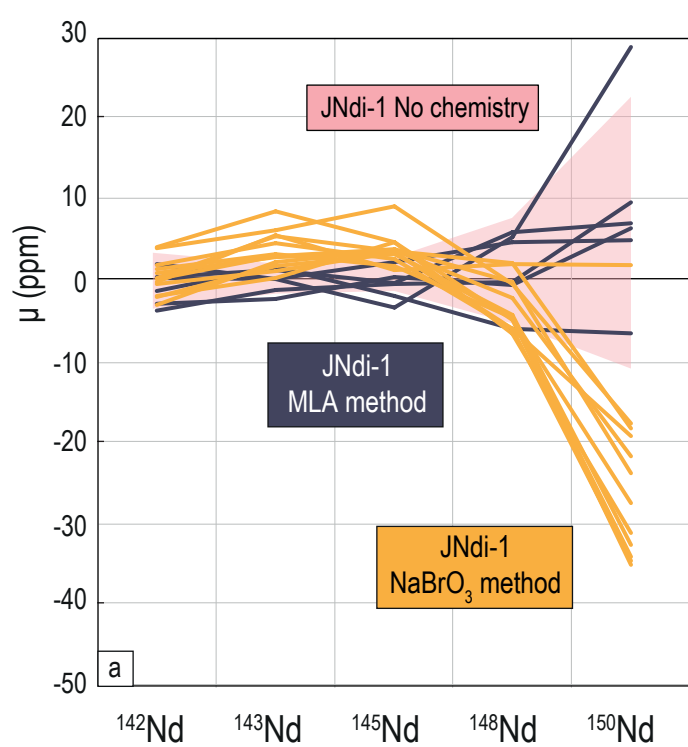
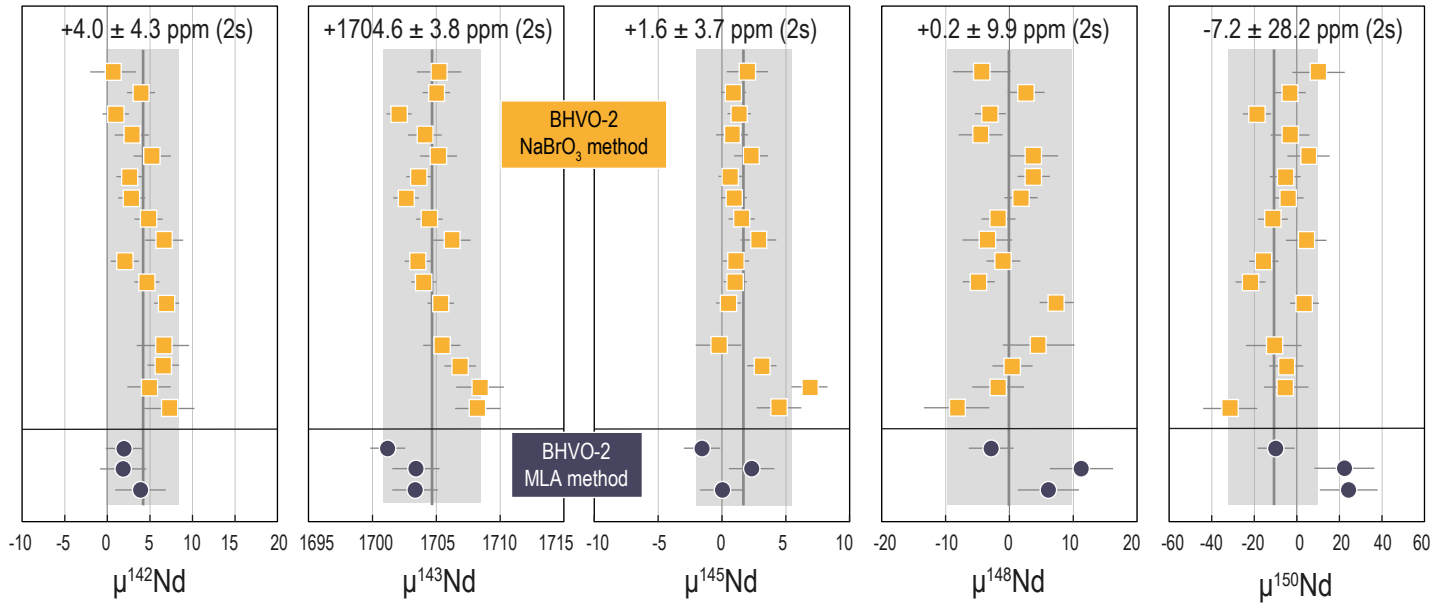


Figure 13

Average dynamic ratios (drift-corrected)



Average dynamic ratios (no correction)

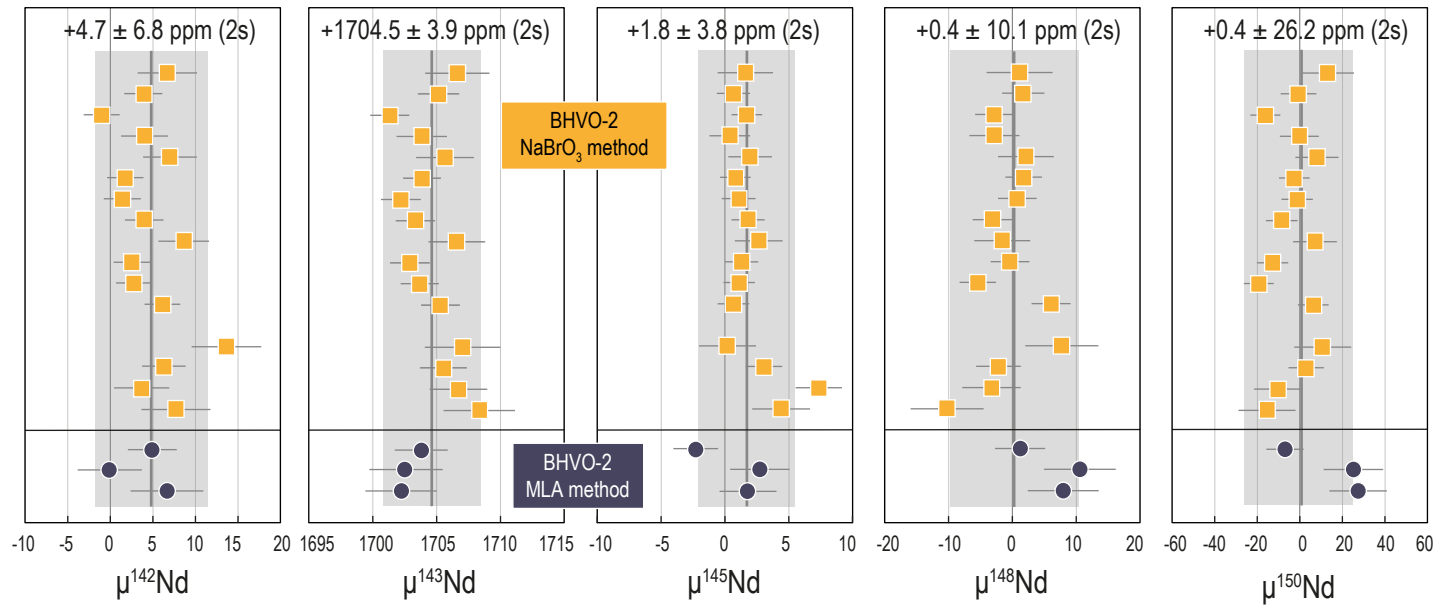
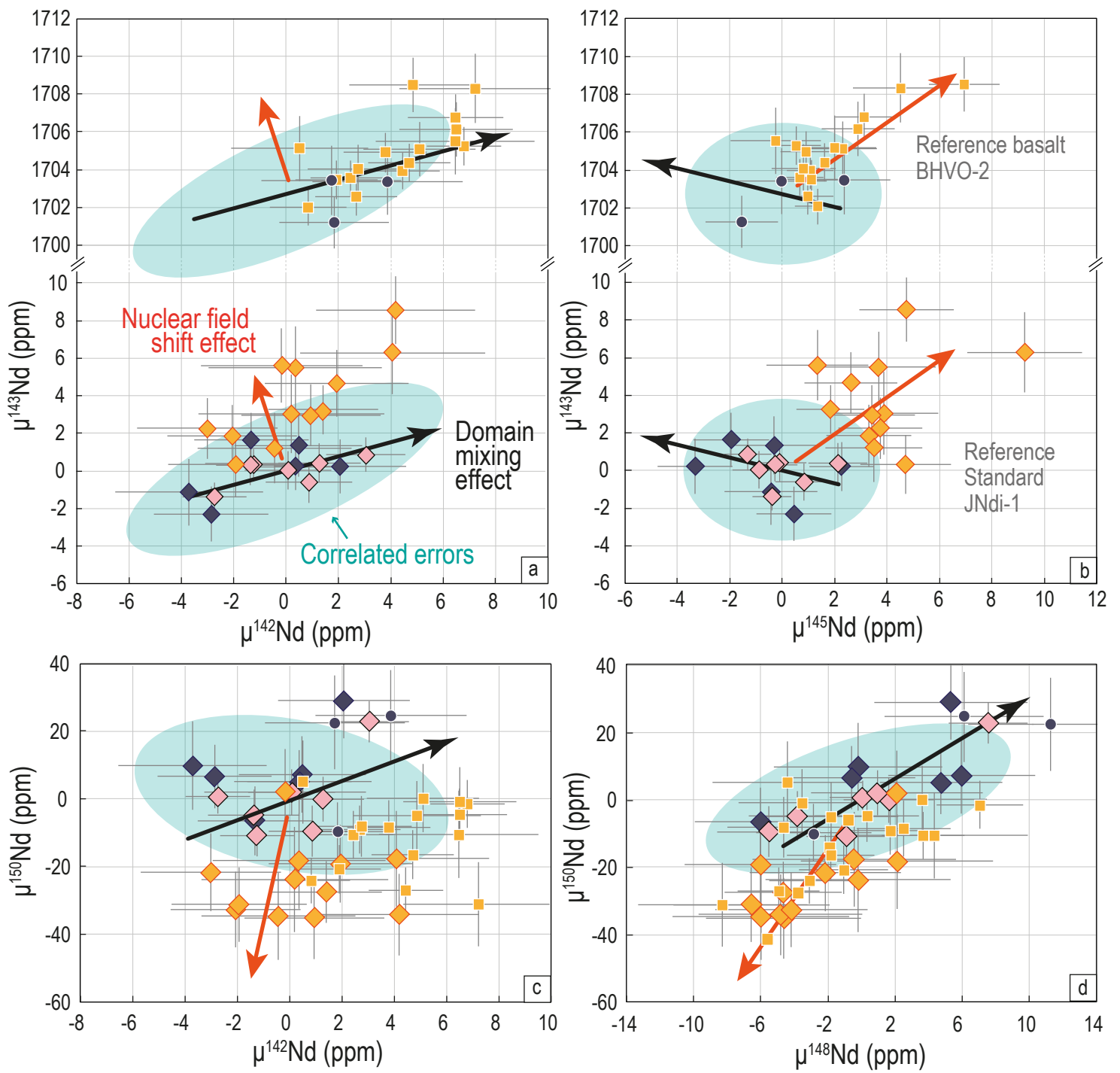


Figure 14



Legend (as in Figures 11 and 13)

□ No chemistry

■ NaBrO₃ method

■ MLA method

○ □ Reference basalt BHVO-2

◇ Reference JNdi-1 Nd standard

Table 1: Collector configuration for the 4 line-method

Configuration 1	Faraday collector									Zoom optics		Idle time (s)	Integration time (s)	Nb of integration	Peak center	Lens focus
	L4	L3	L2	L1	Ax	H1	H2	H3	H4	Focus (V)	Dispersion (V)					
Line 1	139	140	141	142	143	144	145	146	148	-2	8.5	3.0	8.39	1	143	145
Line 2	140	141	142	143	144	145	146	147	149	-1	4	3.0	8.39	1	144	
Line 3	141	142	143	144	145	146	147	148	150	0	0	3.0	8.39	1	145	
Line 4	142	143	144	145	146	147	148	149	151	1	-5	3.0	8.39	1	146	

Configuration 2	Faraday collector									Zoom optics		Idle time (s)	Integration time (s)	Nb of integration	Peak center	Lens focus
	L4	L3	L2	L1	Ax	H1	H2	H3	H4	Focus (V)	Dispersion (V)					
Line 1	139	140	141	142	143	144	145	146	148	-2	8.5	3.0	8.39	1	143	145
Line 3	141	142	143	144	145	146	147	148	150	0	0	3.0	8.39	1	145	
Line 2	140	141	142	143	144	145	146	147	149	-1	4	3.0	8.39	1	144	
Line 4	142	143	144	145	146	147	148	149	151	1	-5	3.0	8.39	1	146	

Table 2 Example of the ratios calculated for each run using our Matlab routine

Sample name F6R1 JNdi-6 Avril 2016
 Number of cycles 540
 Average intensity ^{142}Nd 7.4 V
 Average fractionation rate 0.110 ppm/s

	Static 1	Static 2	Static 3	Static 4	All Static	Dynamic 1	Dynamic 2	Dynamic 3	All Dynamic
$^{142}\text{Nd}/^{144}\text{Nd}$	1.141837	1.141848	1.141826	1.141818	1.141832	1.141832	1.141837		1.141834
2SE	3.94E-06	4.12E-06	3.76E-06	3.75E-06	2.01E-06	3.14E-06	3.13E-06		2.22E-06
$^{143}\text{Nd}/^{144}\text{Nd}$	0.512098	0.512105	0.512096	0.512096	0.512099	0.512100	0.512099		0.512100
2SE	1.42E-06	1.52E-06	1.38E-06	1.48E-06	7.44E-07	1.05E-06	9.59E-07		7.09E-07
$^{145}\text{Nd}/^{144}\text{Nd}$	0.348404	0.348402	0.348400	0.348404	0.348403	0.348403	0.348402	0.348402	0.348402
2SE	8.67E-07	8.68E-07	1.38E-06	9.08E-07	4.45E-07	6.70E-07	6.36E-07	6.74E-07	3.81E-07
$^{148}\text{Nd}/^{144}\text{Nd}$	0.241578		0.241583	0.241584	0.241582	0.241581	0.241581		0.241581
2SE	1.07E-06		1.05E-06	1.06E-06	6.28E-07	8.83E-07	9.03E-07		6.31E-07
$^{150}\text{Nd}/^{144}\text{Nd}$			0.236453			0.236450			0.236450
2SE			1.44E-06			1.29E-06			1.29E-06
$^{146}\text{Nd}/^{144}\text{Nd}$	0.721751	0.721754	0.721747	0.721746					
2SE	6.46E-05	6.47E-05	6.46E-05	6.47E-05					
$^{140}\text{Ce}/^{146}\text{Nd}$	2.03E-06	2.93E-06							
2SE	2.30E-07	2.19E-07							
$^{147}\text{Sm}/^{144}\text{Nd}$		1.90E-07	4.58E-07	1.30E-06					
2SE		1.78E-07	1.77E-07	1.89E-07					
$^{141}\text{Pr}/^{144}\text{Nd}$	4.03E-05	4.17E-05	4.10E-05						
2SE	1.09E-06	1.09E-06	1.11E-06						

Table 3: Suggested reference values for the absolute Nd isotopic composition of the JNdi-1 Nd reference standard measured by TIMS.

	$^{142}\text{Nd}/^{144}\text{Nd}$	2s	2s (ppm)	$^{143}\text{Nd}/^{144}\text{Nd}$	2s	2s (ppm)	$^{145}\text{Nd}/^{144}\text{Nd}$	2s	2s (ppm)	$^{148}\text{Nd}/^{144}\text{Nd}$	2s	2s (ppm)	$^{150}\text{Nd}/^{144}\text{Nd}$	2s	2s (ppm)
Static 1	1.141849	6.5E-05	56.6	0.512103	2.9E-05	56.3	0.348404	1.5E-05	43.0	0.241580	1.9E-05	76.7			
Static 2	1.141853	3.0E-05	26.4	0.512102	9.0E-06	17.6	0.348401	1.4E-05	40.4						
Static 3	1.141840	3.9E-05	34.0	0.512103	1.5E-05	29.8	0.348402	1.2E-05	35.6	0.241585	1.3E-05	53.9	0.236458	1.9E-05	81.9
Static 4	1.141822	2.0E-05	17.8	0.512096	9.0E-06	17.7	0.348402	5.5E-06	15.7	0.241585	7.7E-06	31.7			
All Static (Multi-static)	1.141841	2.0E-05	17.3	0.512101	9.8E-06	19.1	0.348402	3.1E-06	9.0	0.241583	5.0E-06	20.8	0.236458	1.9E-05	81.9
Dynamic 1	1.141835	8.4E-06	7.3	0.512100	6.1E-06	12.0	0.348403	2.8E-06	8.1	0.241582	4.0E-06	16.7	0.236455	6.1E-06	25.9
Dynamic 2	1.141838	8.4E-06	7.4	0.512100	4.5E-06	8.8	0.348402	4.2E-06	12.0	0.241582	4.5E-06	18.6			
Dynamic 3							0.348403	3.8E-06	11.0						
All Dynamic	1.141837	7.2E-06	6.3	0.512100	5.0E-06	9.7	0.348402	3.5E-06	10.0	0.241582	4.0E-06	16.4	0.236455	6.1E-06	25.9
Dynamic 1 drift-corrected	1.141831	8.2E-06	7.2	0.512099	4.7E-06	9.1	0.348403	2.7E-06	7.7	0.241581	3.5E-06	14.4	0.236452	5.5E-06	23.2
Dynamic 2 drift-corrected	1.141833	6.9E-06	6.1	0.512099	4.9E-06	9.5	0.348402	3.9E-06	11.2	0.241581	4.0E-06	16.5			
Dynamic 3 drift-corrected							0.348403	3.8E-06	10.9						
All Dynamic drift-corrected	1.141832	6.4E-06	5.6	0.512099	4.7E-06	9.2	0.348403	3.3E-06	9.6	0.241581	3.4E-06	14.1	0.236452	5.5E-06	23.2

Table 4: Mean dynamic ratios of the JNdi-1 Nd reference standards gathered in 5 groups as a function of the instrument and the age of the faraday cups.

	Triton Carnegie		Triton LMV		Triton PLUS LMV
Analytical sequences	July-Sept 2015	Nov-Dec 2015	Apr-July 2016	Jan-17	Oct-Nov 2016
Age of the faraday cups	18-21 months	22-24 months	2-6 months	11 months	1-2 months
Number of analyses	7	8	23	5	11
Collector configuration	Configuration 1	Configuration 1	Configuration 1	Configuration 2	Configuration 1
<i>No correction</i>					
142Nd/144Nd	1.141839	1.141838	1.141836	1.141833	1.141838
2s	7.3E-06	3.7E-06	7.0E-06	5.5E-06	7.5E-06
2s (ppm)	6.4	3.2	6.1	4.8	6.6
143Nd/144Nd	0.512101	0.512102	0.512100	0.512102	0.512096
2s	3.1E-06	9.5E-07	2.0E-06	1.6E-06	3.3E-06
2s (ppm)	6.2	1.9	4.0	3.1	6.4
145Nd/144Nd	0.348403	0.348404	0.348403	0.348405	0.348400
2s	1.1E-06	1.2E-06	9.7E-07	5.8E-07	9.1E-07
2s (ppm)	3.2	3.4	2.8	1.7	2.6
148Nd/144Nd	0.241581	0.241582	0.241582	0.241579	0.241585
2s	1.7E-06	1.9E-06	2.1E-06	1.2E-06	2.4E-06
2s (ppm)	7.2	7.7	8.8	4.9	9.9
150Nd/144Nd	0.236456	0.236453	0.236454	0.236453	0.236458
2s	5.5E-06	3.8E-06	5.4E-06	4.7E-06	5.6E-06
2s (ppm)	23.4	16.0	23.0	20.0	23.9
<i>Drift corrected</i>					
142Nd/144Nd	1.141835	1.141835	1.141831	1.141830	1.141830
2s	4.8E-06	2.1E-06	5.6E-06	5.1E-06	4.3E-06
2s (ppm)	4.2	1.9	4.9	4.5	3.8
143Nd/144Nd	0.512100	0.512102	0.512099	0.512101	0.512095
2s	3.0E-06	8.6E-07	1.4E-06	1.6E-06	6.1E-07
2s (ppm)	5.8	1.7	2.8	3.0	1.2
145Nd/144Nd	0.348403	0.348404	0.348403	0.348405	0.348400
2s	1.3E-06	9.4E-07	7.9E-07	4.5E-07	8.5E-07
2s (ppm)	3.8	2.7	2.3	1.3	2.4
148Nd/144Nd	0.241581	0.241581	0.241581	0.241578	0.241584
2s	2.2E-06	2.3E-06	1.8E-06	1.2E-06	2.1E-06
2s (ppm)	9.0	9.4	7.6	5.1	8.8
150Nd/144Nd	0.236456	0.236452	0.236451	0.236453	0.236453
2s	5.5E-06	5.3E-06	3.9E-06	4.7E-06	5.3E-06
2s (ppm)	23.4	22.5	16.6	20.0	22.6